Geophysical Journal International

Geophys. J. Int. (2019) **218,** 1761–1780
Advance Access publication 2019 June 03
GJI Seismology

doi: 10.1093/gji/ggz261

Rayleigh-wave multicomponent cross-correlation-based source strength distribution inversion. Part 1: Theory and numerical examples

Zongbo Xu [1], T. Dylan Mikesell [1], Gabriel Gribler[1] and Aurélien Mordret [2]

[1] *Environmental Seismology Laboratory, Department of Geosciences, Boise State University, Boise, ID, USA. E-mail: zongboxu@u.boisestate.edu*
[2] *Department of Earth, Atmospheric, and Planetary Sciences, Massachusetts Institute of Technology, Cambridge, MA, USA*

Accepted 2019 June 1. Received 2019 May 14; in original form 2019 February 20

SUMMARY

Cross-correlation-based seismic interferometry is commonly used to retrieve surface-wave Green's functions from ambient seismic noise recordings. This approach requires that seismic sources are isotropically distributed in all directions around two receivers. However, this assumption is rarely valid in practice. Thus full-waveform inversion theory has recently been applied to seismic noise cross-correlation functions, functions that include both source and structure information. Source information (e.g. location or strength) is essential for accurate structure information estimation. In this paper, we explain physically two types of source sensitivity kernels: one derived from traveltime misfits and the other derived from waveform misfits. We use these kernels for source inversion and demonstrate the benefits of using multicomponent cross-correlations in this source estimation process.

Key words: Waveform inversion; Seismic interferometry; Seismic noise; Surface waves and free oscillations.

1 INTRODUCTION

One nowadays commonly cross-correlates ambient seismic recordings of two sensors to retrieve the surface-wave Green's functions between the two sensors (e.g. Snieder 2004). Assuming the cross-correlation function is the band-limited Green's functions, one can estimate subsurface geologic structures (e.g. Shapiro *et al.* 2005). The cross-correlation method, or seismic interferometry, requires that seismic sources are isotropically distributed in all directions around two receivers (e.g. Wapenaar & Fokkema 2006). However, this assumption is rarely valid in practice. An anisotropic source distribution will bias the retrieved Green's functions and the resulting subsurface geologic inferences (e.g. Yang & Ritzwoller 2008; Yao & van Der Hilst 2009). To reduce this bias, approaches have been developed to compensate for the anisotropic source distribution. For example, one approach uses beamforming (e.g. Rost & Thomas 2002) to estimate the seismic source direction and then uses this direction to correct the retrieved Green's function or surface-wave dispersion estimates (e.g. Nakata *et al.* 2015; Cheng *et al.* 2016). When using beamforming, one assumes that the underground is isotropic and laterally homogeneous. This assumption for the subsurface structures is also not always valid. For anisotropic seismic source distributions and laterally heterogeneous subsurface structures, it has been proposed not to use the seismic cross-correlations to approximate Green's functions, but instead to apply full-waveform inversion theory to the seismic cross-correlations (Tromp *et al.* 2010; Fichtner 2015). The seismic cross-correlations include both source distribution and subsurface structure information. If one wants to estimate the subsurface structure, one has to first (e.g. Nakata *et al.* 2015; Cheng *et al.* 2016), or simultaneously (e.g. Yao & van Der Hilst 2009; Harmon *et al.* 2010), unravel the anisotropic source information.

Source distribution estimation can aid studies of the dynamic processes that generate ambient seismic noise. For example, high-frequency (>1 Hz) ambient seismic noise can be used to monitor underground hydrothermal acoustic sources (e.g. Cros *et al.* 2011) and microseismic sources at the exploration scale (e.g. Corciulo *et al.* 2012); 5–20 s period ambient seismic noise can be used to study the primary and secondary microseisms (e.g. Tian & Ritzwoller 2015; Juretzek & Hadziioannou 2016); 100 s period noise can be used to study the Earth hum (e.g. Rhie & Romanowicz 2006; Nishida & Fukao 2007; Traer & Gerstoft 2014; Ardhuin *et al.* 2015).

Rayleigh waves dominate ambient seismic noise. Multicomponent Rayleigh-wave data can bring benefits for estimating both source distributions and subsurface structures. The important multicomponent data for Rayleigh waves are the vertical (Z) and radial (R) components, where the R direction is parallel to a line or great-circle path between two sensors. If we assume vertical-force seismic sources, the $Z{-}Z$ component cross-correlation (C_{ZZ}) is sensitive to the seismic sources in all directions, while the $R{-}R$ component cross-correlation (C_{RR}) is more sensitive to in-line seismic sources than out-of-line sources (e.g. Haney *et al.* 2012; Xu & Mikesell 2017). Multicomponent data can

also help to characterize Rayleigh waves more accurately than only the *Z*-component data (e.g. Boaga *et al.* 2013; Gribler *et al.* 2016) and constrain the shear-wave velocity inversions (e.g. Arai & Tokimatsu 2004). In this paper, we focus on source estimation rather than structure estimation.

There are mainly two methods for locating seismic sources, an imaging method and an adjoint-based inversion method. When using the imaging method, one applies time reversal to recorded seismic waveforms and then finds the location where the reversed waveforms are most similar to each other. This method includes backprojection (e.g. Ishii *et al.* 2005), reverse-time migration (e.g. Artman *et al.* 2010) and matched-field processing (e.g. Cros *et al.* 2011). These approaches do not involve so-called inversion, as compared to the adjoint-based inversion method. The adjoint-based inversion method combines time reversal and iterative optimization (e.g. Liu *et al.* 2004). When using either of these two methods, one assumes that the subsurface structure is known and then solves for the source parameters (e.g. location or moment tensors). Thus we study multicomponent cross-correlations in the context of ambient noise full-waveform inversion in this paper.

We adopt full-waveform inversion theory to estimate seismic source distributions. We compare the use of traveltime and waveform information in inversion, and we discuss the source sensitivity kernels for C_{ZZ} and C_{RR}. We present the complete inversion scheme in Section 2. In Section 3, we present the kernels for a single frequency and a frequency band, and we explain the physics behind these kernels. We then apply the multicomponent source kernels in three synthetic data examples and estimate the source distributions (Section 4). Finally, we discuss factors that affect the accuracy of the inversions in Section 5.

2 CROSS-CORRELATION INVERSION SCHEME

We use full-waveform inversion theory to estimate seismic source distributions. In an inversion process, we define a misfit function to measure the difference between the synthetic and observed data (Section 2.1). The observed data in this paper are observed Rayleigh-wave cross-correlations. We compute synthetic cross-correlations using a forward modelling process based on the source model parameters, that is the source strength distribution (Section 2.2). We then update the source model parameters with an inversion method that minimizes the misfit function (Section 2.4). This is a common strategy in non-linear inverse problems (e.g. Aster *et al.* 2011).

2.1 Misfit functions

One can define the misfit function (χ) based on physical properties of waveforms, for example traveltimes (e.g. Luo & Schuster 1991; Dahlen *et al.* 2000), envelopes (e.g. Fichtner *et al.* 2008; Bozdağ *et al.* 2011) or raw waveforms (e.g. Tromp *et al.* 2005). Here we use two L_2–norm misfit functions: Rayleigh-wave waveform cross-correlation difference (eq. 1) and Rayleigh-wave traveltime difference (eq. 2). We define the waveform misfit function as

$$\chi = \frac{1}{2}\sum_{mn}\sum_{r_A r_B}\int [w(t)(C_{mn}(r_A, r_B, t) - C^o_{mn}(r_A, r_B, t))]^2 \mathrm{d}t, \tag{1}$$

where $w(t)$ is a time window, and $C_{mn}(r_A, r_B, t)$ and C^o_{mn} are the synthetic and observed cross-correlations, respectively. The cross-correlations are between sensor r_A and r_B; m, n represent the components, vertical (Z) or radial (R), from each of the two sensors, respectively. We use the time window to focus on certain parts of the observed cross-correlations (e.g. Maggi *et al.* 2009; Fichtner *et al.* 2017). We define the traveltime misfit function following Luo & Schuster (1991) as

$$\chi = \frac{1}{2}\sum_{mn}\sum_{r_A r_B}(T_{syn}(r_A, r_B) - T_{obs}(r_A, r_B))^2, \tag{2}$$

where T_{syn} and T_{obs} represent the traveltime of the main Rayleigh-wave waveform in the synthetic and observed cross-correlations, respectively. Luo & Schuster (1991) and Dahlen *et al.* (2000) describe how to measure the traveltime difference, $T_{syn} - T_{obs}$. We restate this measurement procedure in Appendix A. In this paper, we call the source inversions using the waveform and the traveltime misfit functions as the waveform inversion and the traveltime inversion, respectively.

2.2 Forward modelling process

We need synthetic data to calculate the misfit function. We compute synthetic cross-correlations from a source distribution with the forward modelling process. People have discussed the whole forward modelling process explicitly (e.g. Wapenaar & Fokkema 2006; Tromp *et al.* 2010; Fichtner *et al.* 2017). We here review the main steps in the forward modelling process implemented in the frequency domain. We first write the seismic record at one sensor (r_A) due to many sources as

$$U_{mp}(r_A, \omega) = \int_V G_{mp}(r_A, r_s, \omega) F_p(r_s, \omega) dr_s, \tag{3}$$

where $G_{mp}(r_A, r_s, \omega)$ is the Green's function representing the mth component displacement response at location r_A due to a point force in the p direction at the source position r_s, ω is the angular frequency, and $F_p(r_s, \omega)$ is the the source wavelet spectrum. We then cross-correlate two

sensor (r_A and r_B) records as

$$C_{mn}(r_A, r_B, \omega) = U_{mp}(r_A, \omega)U^*_{np}(r_B, \omega)$$
$$= \int_V G_{mp}(r_A, r_s, \omega)G^*_{np}(r_B, r_s, \omega)S_p(r_s, \omega)\mathrm{d}r_s, \tag{4}$$

where the asterisk represents complex conjugation. Here we assume that all seismic sources are independent, thus

$$S_p(r_s, \omega) = F_p(r_s, \omega)F^*_p(r_s, \omega). \tag{5}$$

We note that the source strength, S_p, should be non-negative for all frequencies.

The forward modelling process is computationally expensive. Eq. (4) requires one simulation for one point force source at r_s in the p direction. If we have many seismic sources like traffic, we have to conduct many simulations. Therefore people have proposed to decrease the computation by using wavefield reciprocity (e.g. Tromp *et al.* 2010; Ermert *et al.* 2017). From the reciprocity (e.g. Aki & Richards 2002),

$$G_{mp}(r_A, r_s) = G_{pm}(r_s, r_A), \tag{6}$$

and we can modify the forward simulations by activating seismic sources at sensors (r_A), instead of at real seismic sources (r_s). The number of sensors is normally less than the number of potential seismic sources in the source grid. This decreases the forward computation dramatically.

2.3 Fréchet derivative with respect to source strength

Source inversion requires the Fréchet derivative of the misfit function due to perturbations in the source distribution (e.g. Fichtner 2015; Sager *et al.* 2018). Here we review the steps to derive the Fréchet derivative. First, we write the perturbation of the misfit function due to a perturbation in the synthetic cross-correlation as (e.g. Fichtner 2015)

$$\delta\chi(r_A, r_B) = \int_\omega \delta C_{mn}(r_A, r_B, \omega)f\,\mathrm{d}\omega, \tag{7}$$

where f is the adjoint source. The adjoint source is derived from the misfit function, and we show how we derive the traveltime and waveform adjoint sources in Appendices A and B, respectively.

We then write the perturbation of the synthetic cross-correlation (eq. 4) with a first-order term as

$$\delta C_{mn}(r_A, r_B, \omega) = \int_V G_{mp}(r_A, r_s, \omega)G^*_{np}(r_B, r_s, \omega)\delta S_p(r_s, \omega)\mathrm{d}r_s$$
$$+ \int_V \delta[G_{mp}(r_A, r_s, \omega)G^*_{np}(r_B, r_s, \omega)]S_p(r_s, \omega)\mathrm{d}r_s, \tag{8}$$

where the first part in the right hand side is for perturbations in the source, and the second part is for perturbations in the Green's functions. These two parts provide Fréchet source and structure derivatives (Fichtner 2015). We focus on the source derivative in this paper; thus we assume that the subsurface structure and the Green's functions are known, such that $\delta[G_{mp}(r_A, r_s, \omega)G^*_{np}(r_B, r_s, \omega)] = 0$. This assumption is common in source studies (e.g. Liu *et al.* 2004; Ishii *et al.* 2005; Artman *et al.* 2010). We thus write the perturbation of the cross-correlation with respect to source strength perturbations as

$$\delta C_{mn}(r_A, r_B, \omega) = \int_V G_{mp}(r_A, r_s, \omega)G^*_{np}(r_B, r_s, \omega)\delta S_p(r_s, \omega)\mathrm{d}r_s. \tag{9}$$

We then write the Fréchet derivative of the misfit function due to perturbations in the source strength by combining eqs (7) and (9) as

$$\delta\chi(r_A, r_B) = \int_\omega \int_V G_{mp}(r_A, r_s, \omega)G^*_{np}(r_B, r_s, \omega)\delta S_p(r_s, \omega)f\,\mathrm{d}r_s\mathrm{d}\omega, \tag{10}$$
$$= \int_\omega \int_V K_{mn}(r_A, r_B, \omega)\delta S_p(r_s, \omega)\mathrm{d}r_s\mathrm{d}\omega, \tag{11}$$

where

$$K_{mn}(r_A, r_B, \omega) = G_{mp}(r_A, r_s, \omega)G^*_{np}(r_B, r_s, \omega)f. \tag{12}$$

K_{mn} is called the source kernel (e.g. Fichtner *et al.* 2017). The kernel indicates the sensitivity of the misfit function to the source strength S_p at r_s. In practice, it is often assumed that the spectral shapes for all sources (S_p) are similar (e.g. Ermert *et al.* 2017). Thus we assume that $S^0_p N = S_p$, where S^0_p is the assumed source spectrum and N is a ratio. N is always positive due to eq. (5). Finally, we rewrite eqs (11) and (12) as

$$\delta\chi(r_A, r_B) = \int_\omega \int_V K_{mn}(r_A, r_B, \omega)\delta N(r_s)\mathrm{d}r_s\mathrm{d}\omega \tag{13}$$

with

$$K_{mn}(r_A, r_B, \omega) = G_{mp}(r_A, r_s, \omega)G^*_{np}(r_B, r_s, \omega)S^0_p f \tag{14}$$
$$= [G_{mp}(r_A, r_s, \omega)F^0_p][G_{np}(r_B, r_s, \omega)F^0_p]^* f, \tag{15}$$

Table 1. The homogeneous and isotropic elastic halfspace model parameters used in the simulation.

Model	*Vp* ($m\,s^{-1}$)	*Vs* ($m\,s^{-1}$)	Density ($kg\,m^{-3}$)	Thickness (m)
True	2800	1500	2300	∞
Higher	3800	2000	2300	∞
Lower	1900	1000	2300	∞

where $S_p^0 = F_p^0(F_p^0)^*$. Eq. (15) is convenient to use because we can easily compute synthetic seismic recordings ($G_{mp}F_p^0$) with the same numerical simulations used to create synthetic cross-correlation functions. Thus in the following context, we use $N(r_s)$ as the source strength distribution model and use eq. (15) to calculate source sensitivity kernels.

2.4 Inversion strategy

We use a gradient-descent strategy (e.g. Ermert *et al.* 2017), which is an iterative method. The traveltime misfit function (eq. 2) is a non-linear problem and thus requires an iterative method. We can, however, minimize the waveform L2–norm misfit function (eq. 1) using direct methods because the source strengths are linearly related to the crosscorrelation waveforms in the frequency domain (eq. 4). While it is useful to recognize this last point, the waveform misfit function can be too large to solve with linear inversion methods directly due to the potential for a large number of waveforms and source locations. Thus iterative methods are a better option for the sake of memory in such large problems (e.g. Aster *et al.* 2011), and we choose to solve the waveform misfit function with the same iterative method as the traveltime mistfit function. Another way to address this problem is using the adjoint operator (e.g. Thorson & Claerbout 1985), for example, the matched-field processing method (e.g. Cros *et al.* 2011; Corciulo *et al.* 2012) and microseismic reverse-time migration (e.g. Artman *et al.* 2010). We discuss the link between the waveform inversion, matched-field processing, and reverse-time migration methods in Appendix C.

In the waveform inversion, we sum the kernels among all sensor pairs in a frequency band $[\omega_1, \omega_2]$ as

$$K = \sum_{mn}\sum_{r_A r_B}\int_{\omega_1}^{\omega_2} K_{mn}(r_A, r_B, \omega)\mathrm{d}\omega. \tag{16}$$

If we only use vertical data, K is a summed K_{ZZ} among all sensor pairs; if we use both C_{ZZ} and C_{RR}, $K = K_{ZZ} + K_{RR}$ among all sensor pairs. We then multiply the summed kernel (K) with a step size (p) to update the source distribution in the ith iteration as

$$N_{i+1}(r_s) = N_i(r_s) - pK. \tag{17}$$

However, if we subtract the product (pK) directly, negative source strength values may appear. A negative source strength is not physical because of eq. (5). Thus we need to make sure that the updated source strengths are non-negative. To achieve this, we apply a positivity constraint (Johansen 1977) to the inversion, where $\delta ln[N(r_s)] = \delta N(r_s)/N(r_s)$. Rearranging this relationship and replacing $\delta N(r_s)$, eq. (13) becomes

$$\delta\chi(r_A, r_B) = \sum_{mn}\sum_{r_A r_B}\int_{\omega}\int_{V} K_{mn}(r_A, r_B, \omega)N(r_s)\delta ln[N(r_s)]\mathrm{d}r_s\mathrm{d}\omega, \tag{18}$$

where ln is the natural logarithm. We then update the source strength distribution as

$$ln[N_{i+1}(r_s)] = ln[N_i(r_s)] - pN_i(r_s)K, \tag{19}$$

which is equivalent to

$$N_{i+1}(r_s) = N_i(r_s)e^{-pN_i(r_s)K}, \tag{20}$$

and where the exponential term is always positive, thus ensuring the source model will always be positive as long as the starting model is positive.

We choose the step size (p) from many potential step size values. We update the source strength distribution (N_i) using eq. (20) and the potential step sizes (e.g. $p = 10^{-6}, 10^{-5}, ...10^{-1}$). For each step size, we have an updated source distribution model (N_{i+1}), and we compute synthetic cross-correlations using eq. (4). We then calculate the corresponding misfit function. Among these misfit values, we choose the step size that gives the minimum misfit. If the minimum misfit is less than an update criteria (C_u), we adopt the step size and update the source model; if not, we do not update this iteration and instead expand the frequency band. Details about the actual inversion algorithm are presented in Section 4.

3 RAYLEIGH-WAVE SOURCE KERNELS

We present and describe the source kernels for Rayleigh waves of multicomponent cross-correlations (C_{ZZ} and C_{RR}). In calculating the kernels, we require synthetic seismic recordings and adjoint sources (eq. 15). We use a homogeneous elastic halfspace model (Table 1, True model) and SPECFEM3D (Komatitsch & Tromp 2002) to simulate the synthetic seismic recordings. We set the model to be a 3-km-length cube. We

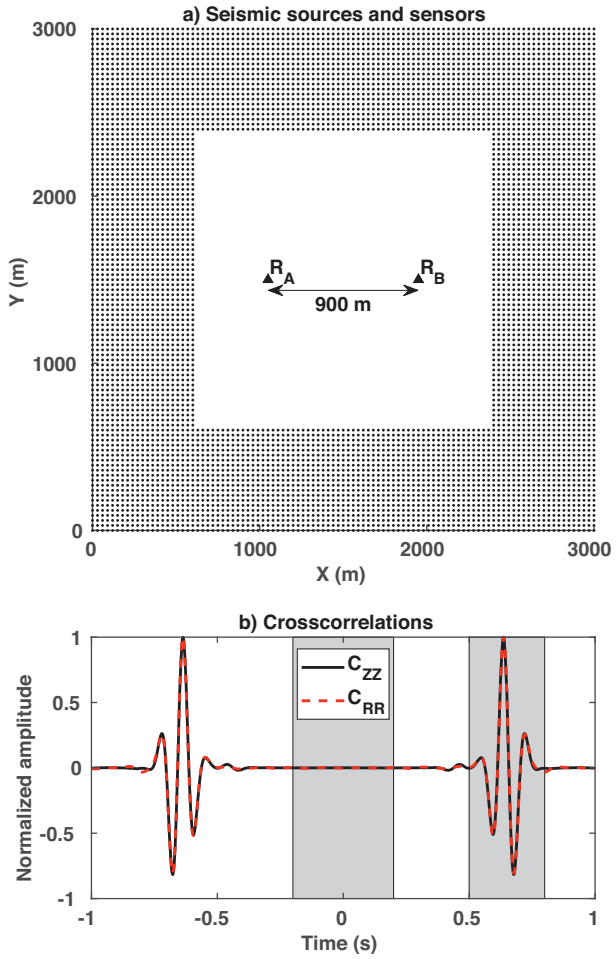

Figure 1. (a) Diagram of locations of the 6720 point sources and two receivers on the free surface. The black points represent point sources; the two black triangles represent the two receivers, r_A and r_B. (b) The vertical–vertical (C_{ZZ}) and radial–radial (C_{RR}) cross-correlation between the two receivers due to all sources in (a). The two cross-correlations are normalized by each maximum amplitude. The two grey blocks indicate two time windows, −0.2 to 0.2 and 0.5 to 0.8 s.

set the top surface of the cube to be a free surface and the other surfaces to be perfectly matched layers. We discretize the whole cube into 30-m-length cubes. In one simulation, the time step is 0.0005 s and we propagate signals for 5000 time steps (i.e. 2.5 s). We simulate Z and R component data on the two receivers (r_A and r_B) due to 6720 vertical-point-force sources on the free surface (Fig. 1a). Each source emits a 10 Hz Ricker wavelet with an amplitude factor of 10^{15} in SPECFEM3D [F_z in eq. (5), also F_z^0 in eq. (15)]. Following Section 2.2, we do 4 simulations ($Z-$ and $R-$ direction point forces at each receiver), and record at the 6720 seismic source locations. We compute C_{ZZ} and C_{RR} (eq. 4). The phase of C_{ZZ} is identical to that of C_{RR} (Fig. 1b).

We focus on the sensitivity kernels for synthetic data in this section to study the kernel structure. Therefore we use two modified misfit functions:

$$\chi(r_A, r_B) = T_{syn} \tag{21}$$

and

$$\chi(r_A, r_B) = \frac{1}{2}\int [w(t)C_{mn}(r_A, r_B, t)]^2 \mathrm{d}t. \tag{22}$$

These two misfit functions indicate the traveltime and energy for main waveforms in the synthetic cross-correlations, respectively (Fichtner *et al.* 2017). The corresponding adjoint sources are presented in Appendices A and B. The corresponding source kernels determine how source strength changes affect the traveltime or waveform energy.

3.1 Monochromatic source kernels

We now describe the monochromatic cross-correlation source kernels from a physical point of view. In a homogeneous and isotropic medium, under the far-field assumption, the vertical-component fundamental-mode Rayleigh-wave Green's function due to a vertical point force can

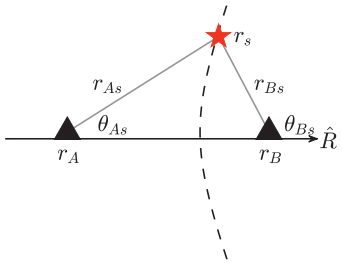

Figure 2. Diagram of the location of a point source (star) and two sensors (triangles). The dashed hyperbola indicates potential source locations, where $r_{As} - r_{Bs}$ is constant. The radial direction, $\hat{R}$, is parallel to the line linking the two sensors, r_A and r_B.

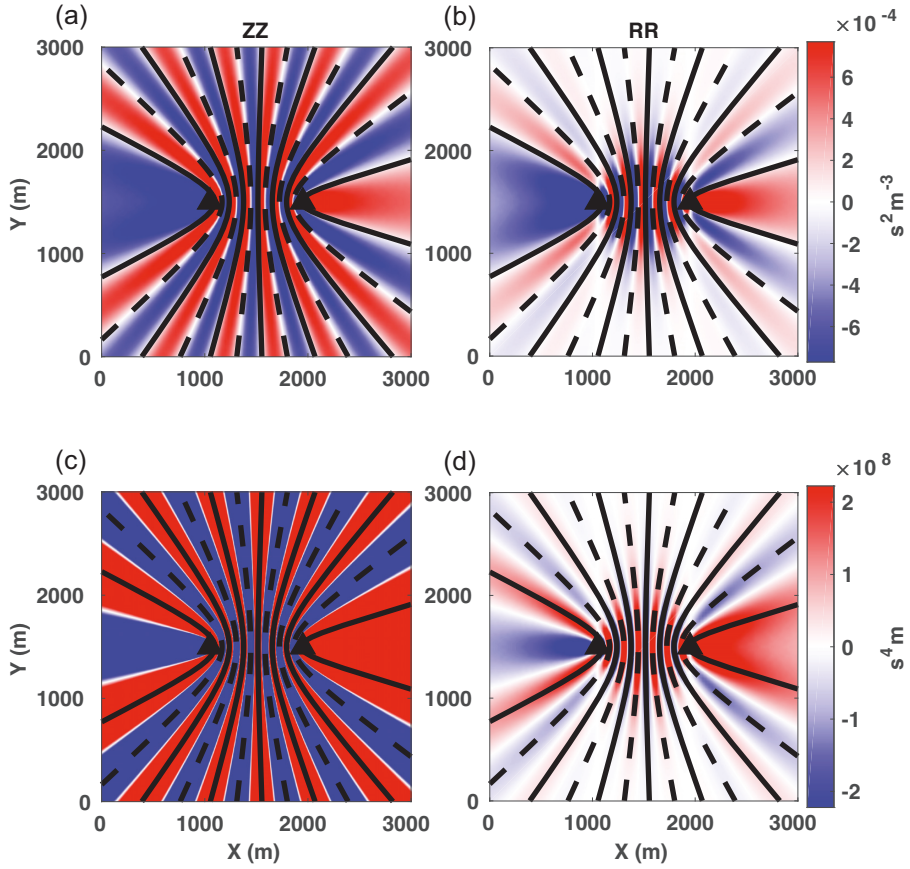

Figure 3. Traveltime (top row) and waveform-energy (bottom row) source kernels computed at each grid node for 5 Hz direct Rayleigh waves in the causal parts of C_{ZZ} (left-hand column) and C_{RR} (right-hand column). The solid hyperbolas represent $2N\pi$ phase and the dashed represent $(2N-1)\pi$. The direct Rayleigh-wave time window is from 0.5 to 0.8 s in Fig. 1. These hyperbolas are asymmetric due to the value of ϕ_{obs} in eqs (27) and (28).

be written as (e.g. Fan & Snieder 2009):

$$G_{ZZ}(r,\omega) = \sqrt{\frac{1}{8\pi\omega r/c}}e^{-i(\omega r/c+\pi/4)}, \tag{23}$$

where ω is the angular frequency, i is the imaginary unit, c is the surface-wave phase velocity and r is the distance between source and receiver. The negative sign in the exponential part of eq. (23) is due to the Fourier transform convention we use (Appendix D). If we consider a vertical-point-force seismic source on the free surface at r_s, the surface-wave cross-correlation between two sensors (r_A and r_B) can be written as

$$C_{ZZ}(r_A, r_B, \omega, r_s) = \frac{1}{8\pi\omega/c}\sqrt{\frac{1}{r_{As}r_{Bs}}}e^{-i\omega(r_{As}-r_{Bs})/c}. \tag{24}$$

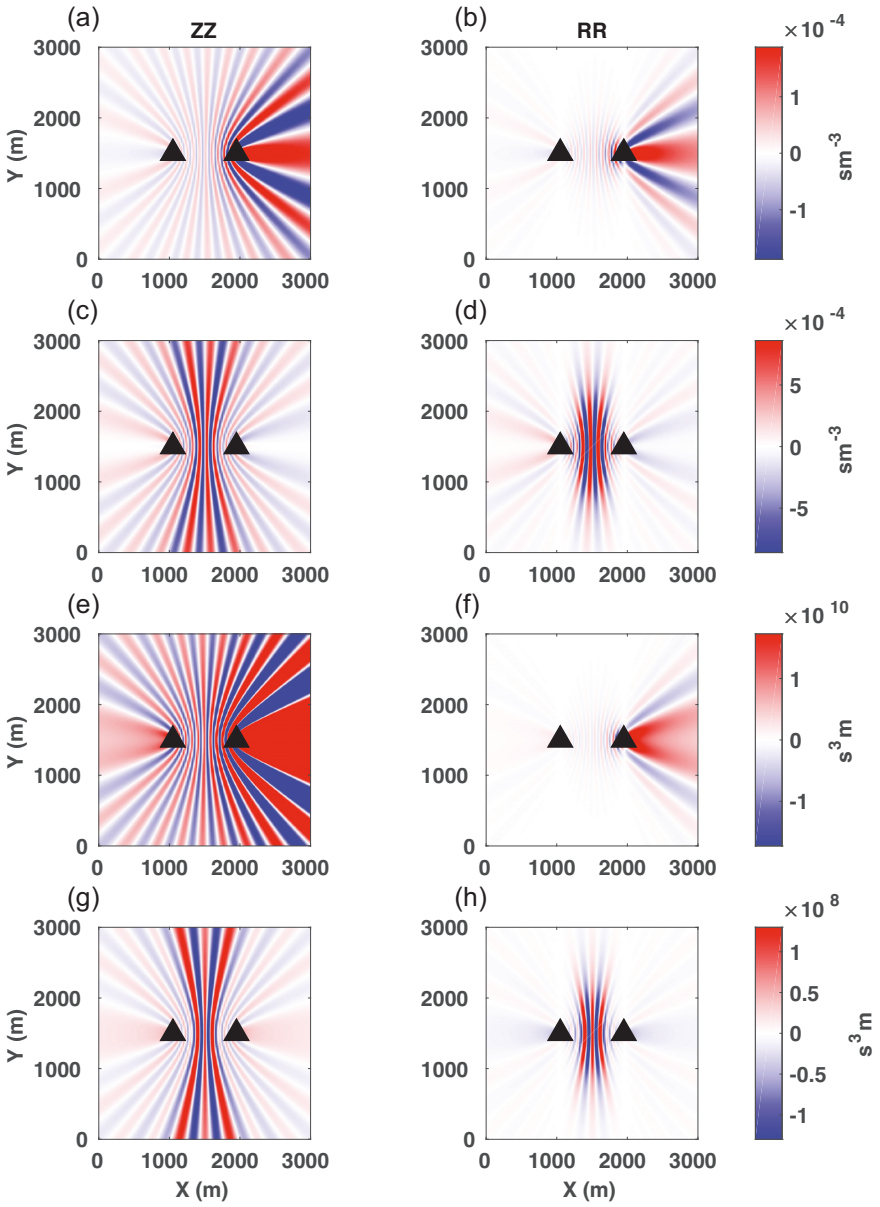

Figure 4. 2–8 Hz traveltime (a, b, c, d) and waveform-energy (e, f, g, h) source kernels for Rayleigh waves in C_{ZZ} (left-hand panel) and C_{RR} (right-hand panel). a, b, e, f are for direct Rayleigh waves (0.5–0.8 s in Fig. 1b); c, d, g and h are for early-arrival Rayleigh waves (–0.2 to 0.2 s in Fig. 1b).

Following the same logic, and using

$$G_{RZ}(r,\omega) = \frac{H}{V}\sqrt{\frac{1}{8\pi\omega r/c}}e^{-i(\omega r/c-\pi/4)}, \tag{25}$$

where H/V is the ratio of the horizontal-to-vertical motion (e.g. Haney *et al.* 2012), we can write

$$C_{RR}(r_A, r_B, \omega, r_s) = \left(\frac{H}{V}\right)^2 \frac{1}{8\pi\omega/c}\sqrt{\frac{1}{r_{As}r_{Bs}}}cos(\theta_{As})cos(\theta_{Bs})e^{-i\omega(r_{As}-r_{Bs})/c}, \tag{26}$$

where θ_{As} is the angle between the surface-wave propagation path and the radial direction (Fig. 2). The phase of the Rayleigh wave is $-\omega(r_{As} - r_{Bs})/c$ in eqs (24) and (26). These phases remain constant if $r_{As} - r_{Bs}$ remains constant; $r_{As} - r_{Bs}$ will be constant if r_s is on a hyperbola with foci at r_A and r_B (Fig. 2). Thus a certain phase corresponds to a hyperbola, comprised of r_s locations. For C_{ZZ} and C_{RR}, we focus on two specific phases:

$$-\frac{\omega(r_{As} - r_{Bs})}{c} = \phi_{obs} + 2N\pi, \tag{27}$$

Table 2. Traveltime and waveform inversion scheme details.

	Traveltime	Waveform
Frequency band used in calculating misfit function and kernel	2–4/6/8/12/16 Hz	
Time window	0.6 s centered at the peak of cross-correlation	−1 to 1 s
Cross-correlation normalization term	Maximum in all C_{ZZ} or C_{RR}	
Smooth source strength per iteration	Yes	No
Update criteria, C_u	100 per cent	99 per cent
Stop criteria, C_s	0.01	0.01

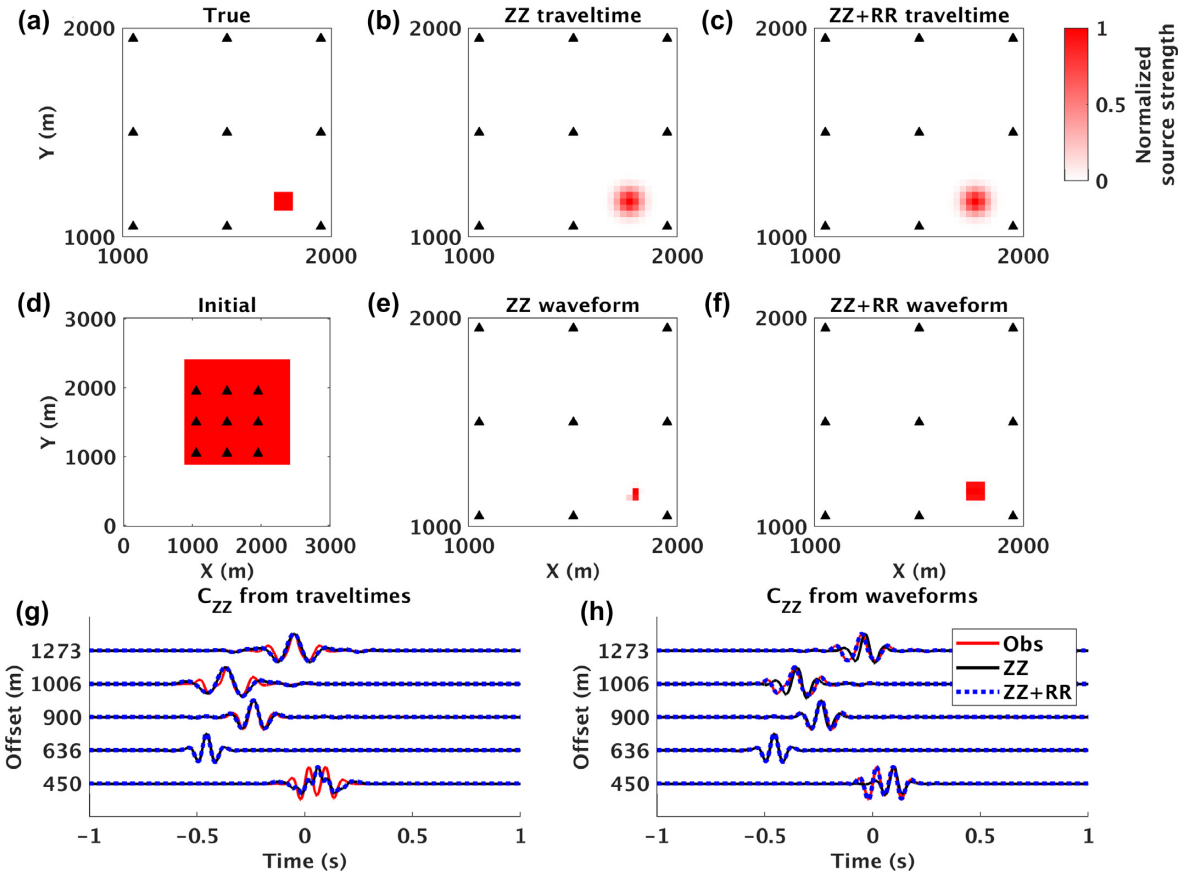

Figure 5. One source within array inversion results and the corresponding C_{ZZ} waveforms. (a) The true source strength distribution is zero everywhere except an in-array source area (square). Triangles are receivers. From the initial seismic source distribution model (d), we invert with the ZZ traveltimes (b), $ZZ + RR$ traveltimes (c), ZZ waveforms (e) and $ZZ + RR$ waveforms (f). We plot the synthetic C_{ZZ} based on the traveltime inversion results in (g) and the waveform inversion results in (h), along with the observed C_{ZZ}. Each waveform here is normalized by its maximum amplitude for comparison. Note that the initial source strength (d) at each receiver location is zero and is masked by the triangles.

and

$$-\frac{\omega(r_{As}-r_{Bs})}{c}=\phi_{obs}+(2N-1)\pi, \tag{28}$$

where ϕ_{obs} is the phase of the observed waveform at $N=0, \pm1, \pm2, \pm3...$ and frequency ω. The two phases lead to two kinds of hyperbolas (Fig. 3): $\phi_{obs}+2N\pi$ phase leads to the same phase (ϕ_{obs}); the $\phi_{obs}+(2N-1)\pi$ leads to the opposite phase ($\phi_{obs}\pm\pi$). These hyperbolas are determined by the value of ϕ_{obs}, which also change with frequency (e.g. Xu *et al.* 2017).

These two kinds of cross-correlations contribute ±1 to the amplitude spectrum, but 0 to the phase spectrum of the Rayleigh wave in C_{ZZ} over the time window $w(t)$. If we increase or decrease the source strength along one of these hyperbolas, the arrival time of the Rayleigh waveform will not change because the corresponding phase spectrum does not change; however, the waveform energy will increase or decrease, respectively. This is because the sources along the hyperbola generate waveforms with exactly the same phase and arrival time. Therefore the hyperbola is located along the zero value in the traveltime kernels, and along the maxima and minima of the waveform-energy kernels (Fig. 3). Chmiel *et al.* (2018) observed similar source kernels with dense active-source seismic recordings and calculated the surface-wave phase velocities by fitting hyperbolas to the kernels using eqs (27) and (28).

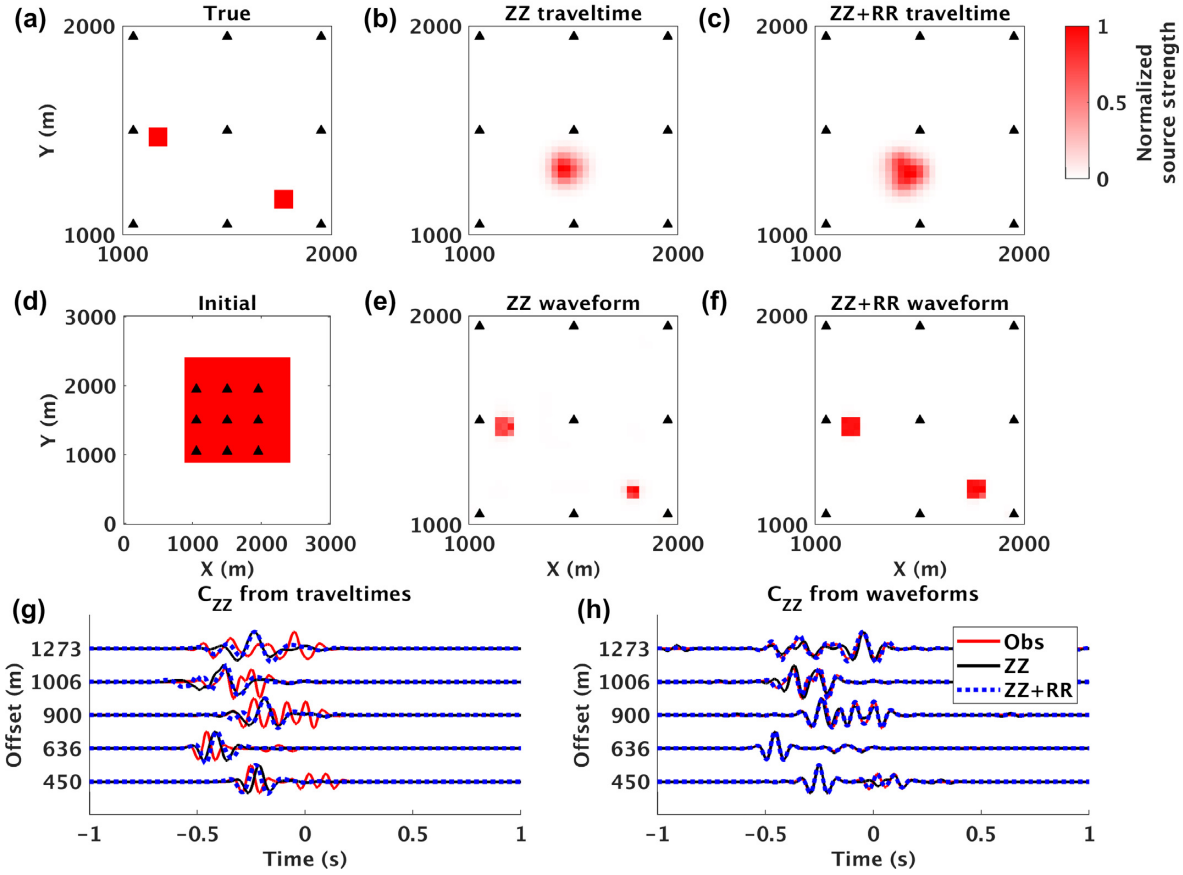

Figure 6. Two sources within array inversion results and the corresponding waveforms. (a) The true source strength is zero everywhere except two source areas (squares) within the array (triangles). From the same initial source distribution model (d) as in Fig. 5, we invert the *ZZ* traveltimes (b), $ZZ + RR$ traveltimes (c), *ZZ* waveforms (e) and $ZZ + RR$ waveforms (f). We plot the synthetic C_{ZZ} based on the traveltime inversion results in (g) and the waveform inversion results in (h), along with the observed C_{ZZ}. Each waveform here is normalized by its maximum amplitude for comparison. Note that the initial source strength (d) at each receiver location is zero and is masked by the triangles.

We point out that the traveltime and waveform kernels for *RR* are stronger in the in-line areas than out-of-line areas (Figs 3b and d). This azimuthal effect is due to the $cos(\theta_{As})cos(\theta_{Bs})$ term in eq. (26). Xu & Mikesell (2017) observed this effect and noted that this effect is frequency independent. The *cos* term can change sign with the receivers. Therefore the *RR* kernels can also change the sign of the kernel values, even if r_s moves along the same hyperbola as seen in Figs 3b and 3d. The absolute amplitude difference in the sensitivities between *ZZ* and *RR* kernels is due to the *H*/*V* ratio (eq. 26). Depending on the subsurface model, this indicates that either the *ZZ* or *RR* kernel could dominate the stacked kernel (eq. 16) at a particular frequency depending on the *H*/*V* ratio.

3.2 Multi-frequency source kernels

We stack the monochromatic source kernels over a frequency band, during which monochromatic kernels interfere with each other. In areas where these kernels share common sensitivity, the magnitude of sensitivity increases due to stacking. In other areas, the kernels destructively interfere and the magnitude decreases. Therefore, we observe that the direct Rayleigh waves in C_{ZZ} and C_{RR} are sensitive to sources in the in-line areas (Figs 4a, b, e and f), the so-called stationary-phase zone (e.g. Snieder 2004). In this case we observe the majority of the sensitivity on the right-hand side of the model because we use a time window around the causal direct Rayleigh waves (Fig. 1b). If we increase the in-line source strength, the traveltime and waveform energy will increase. This expectation fits the sensitivity sign in the in-line areas (Figs 4a, b, e and f). For arrivals near the zero-time location (Fig. 1b), we observe that both *ZZ* and *RR* taveltime and waveform-energy kernels are sensitive to seismic sources between the two sensors (Figs 4c, d, g and h).

We also observe the azimuthal effect in the *RR* kernels. Compared to the *ZZ* source kernels (Figs 4a, c, e and g), the *RR* source kernels (Figs 4b, d, f and h) possess less sensitivity to sources on the sidelobe areas. Thus for direct Rayleigh waves, we can use *RR* to focus on in-line seismic sources (Figs 4b and f) and decrease the error in Rayleigh-wave dispersion measurements due to anisotropic source distributions (e.g. van Wijk *et al.* 2011; Haney *et al.* 2012; Xu & Mikesell 2017). For Rayleigh waves near the zero point in cross-correlations, where seismic sources occur between sensors, *RR* should help to locate the sources better than *ZZ* (Figs 4d and h versus c and g).

4 SOURCE ESTIMATION SYNTHETIC EXAMPLES

We present three synthetic source inversion examples to demonstrate that multicomponent cross-correlations (C_{RR} and C_{ZZ}) better estimate anisotropic source distributions than C_{ZZ}. We use nine sensors in a square array in all examples. The smallest distance between two adjacent sensors is 450 m. We assume that all seismic sources are distributed on the free surface. In the first two examples, the seismic sources occur within the array area, with the sources distributed outside of the array in the third example. Each source emits a 10 Hz Ricker wavelet with an amplitude factor of 10^{15}. The subsurface is the same homogeneous medium (Table 1, True model) as in Section 3. We assume that we know the subsurface structure and the source wavelet in the inversions. Thus we simulate the observed and synthetic cross-correlations following Section 3. We use the simulated wavefield to calculate the source kernels (eq. 15). We use both C_{ZZ} and $C_{ZZ} + C_{RR}$ in the inversions with waveform and traveltime misfit functions (eqs 1 and 2). In using $C_{ZZ} + C_{RR}$ in misfit functions, we weight the cross-correlaions by normalizing the amplitudes of C_{ZZ} and C_{RR} by the corresponding C_{ZZ} and C_{RR} waveform maxima of all sensor pairs, respectively. We do this to both synthetic and observed data using their respective maxima. As a consequence, we scale the *ZZ* and *RR* waveform kernels by the synthetic C_{ZZ} and C_{RR} waveform maxima, respectively. We conducted the inversions without scaling the kernels and achieved similar results; however, to keep the system of equations self-consistent the kernels should be scaled in the same way the waveforms are scaled.

We present the entire inversion algorithm as pseudocode (Algorithm 1). We adopt the frequency band extension strategy (e.g. Virieux & Operto 2009). We use a large time window in the waveform inversion (Table 2) because in the cross-correlations the Rayleigh waves can arrive between time zero and the direct-wave arrival time, depending on the different source locations (e.g. Wapenaar & Fokkema 2006). This time-windowing strategy is in contrast to global earthquake seismology where we have accurate predictions of arrival times for body waves and Rayleigh waves (e.g. Maggi *et al.* 2009). If we use a narrow time window in the waveform inversion, artefacts appear outside the narrow time windows. However, the narrow time window works well for the traveltime inversion, because the traveltime inversion simply move waveforms forward or backward in time and thus no artefacts appear. We use the same frequency band to calculate the waveform source kernels and waveform misfit (eq. 1). We measure the traveltime misfits (eq. 2) over the whole frequency band because this measurement is more robust than in narrow frequency bands. We set the initial source strength at each sensor location to be zero, so we can avoid singularities at receivers. We smooth the source strength distributions in the traveltime inversions (see Algorithm 1), but not in the waveform inversions, because the traveltime source kernels possess narrower sensitivity bands than the waveform kernels (Figs 3 and 4). In practice, it is common to smooth the model parameters or gradients in wave-equation based tomography (e.g. Tape *et al.* 2007) and active-source waveform inversion (e.g. Groos *et al.* 2017). The inversion results are normalized by the maximum source strength, because we focus on relative source strength distributions, instead of absolute strength distributions.

Algorithm 1 Inversion algorithm

Normalize observed crosscorrelations by global maximums in C_{ZZ} and C_{RR};
for ith iteration **do**
  forward source distribution model on N_i using eq. (4) and normalize crosscorrelations;
  calculate the misfit, χ_i, over time window using eq. (1) (waveform) or eq. (2) (traveltime);
  calculate adjoint source, f, using eq. (B3) (waveform) or eq. (A9) (traveltime);
  calculate the kernel, K, using eq. (15);
  for each step size, p_j **do**
    update N_i with p_j using eq. (20), (smoothing the updated source model with a 30 m 2D Gaussian filter in the traveltime inversion);
    forward model using source distribution and eq. (4);
    normalize crosscorrelations;
    calculate the misfit, χ_j;
  find the minimum misfit, $min(\chi_j)$, and the corresponding p_j ;
  if $min(\chi_j) < C_u \chi_i$ **then**
    update N_i and achieve N_{i+1} using eq. (20),(smoothing the updated source model with a 30 m 2D Gaussian filter in the traveltime inversion);
  else
    extend frequency band
  In the last frequency band
  if $|N_{i+1} - N_i|/|N_i| < C_s$ **then**
    stop inversion

4.1 Example 1: One source within array

The sensors surround one source area in this case (Fig. 5a). The inversion results (Figs 5b, c, e and f) estimate the source locations and strengths accurately, although the initial source distribution model (Fig. 5d) is far from the true source model. We observe that the inverted

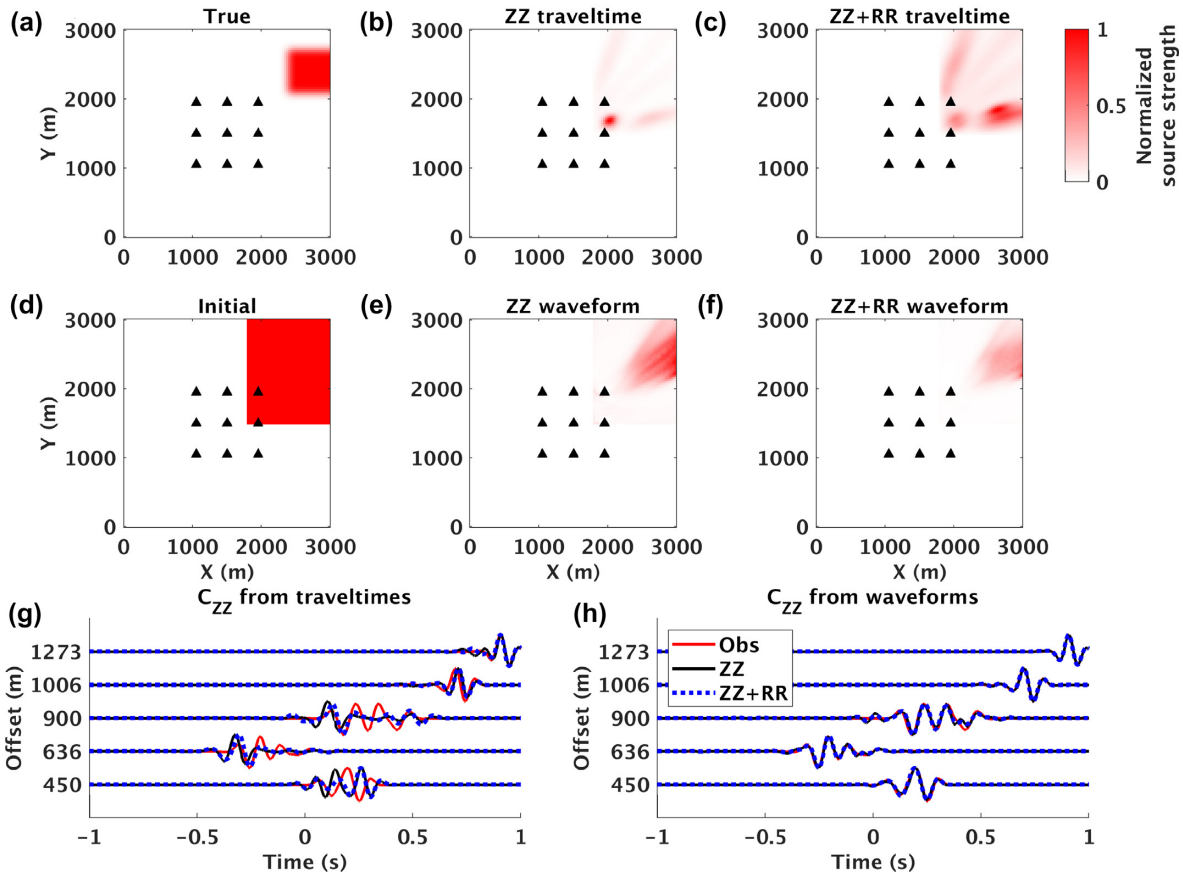

Figure 7. Source out-of-array inversion and the corresponding waveforms. (a) The true source strength is zero everywhere except the out-of-array source area (square). From an initial source model (d), we invert the *ZZ* traveltimes (b), $ZZ + RR$ traveltimes (c), *ZZ* waveforms (e) and $ZZ + RR$ waveforms (f). We plot the synthetic C_{ZZ} based on the traveltime inversion result in (g) and based on the waveform inversion result in (h), along with the observed C_{ZZ}. Each waveform here is normalized by its maximum amplitude for comparison.

source distribution from the waveform inversion (Figs 5e and f) are closer to the true source distribution than from the traveltime inversion (Figs 5b and c); the synthetic waveforms (Fig. 5h) from the waveform inversion results also fit the observed C_{ZZ} better. This is because the waveforms contain not only traveltime information, but also information such as relative amplitudes. Thus, the waveform inversion performs better than the traveltime inversion. We note that the multicomponent data does not improve the source distribution estimation when we only use traveltime information. The $ZZ + RR$ traveltime inversion gives a similar source estimation to the *ZZ* inversion. However, multicomponent data do help constrain the waveform inversion. In the waveform inversions, $ZZ + RR$ better estimates the source shape than *ZZ* alone. Moreover, the synthetic C_{ZZ} waveforms from the multicomponent inversion are closer to the waveforms of the observed C_{ZZ} (Figs 8g and h).

4.2 Example 2: Two sources within array

Two sources in the array make the observed cross-correlation waveforms more complex than in the one-source case. We observe that more arrivals exist in the cross-correlations from the two-source area (Fig. 6h) than from one-source area (Fig. 5h). We use the same initial source model as in the one-source case. The initial source strength model is far away form the true source model, so the corresponding synthetic waveforms are not similar to the observed waveforms. As the traveltime inversion mainly moves waveforms on the time axis, the synthetic waveforms from the traveltime inversion do not fit the observed data. For complex waveforms in the observed data (Fig. 6g), where there are more than one arrival, we determine that the synthetic data from the traveltime inversions will not fit the observed data. Thus the traveltime inversion gives incorrect, single-location estimations (Figs 6b and c). However, the waveform inversion can handle the complex observed data because the waveform inversion can fit multiple arrivals. We estimate accurate source locations and relative strengths with the waveform inversion, and the synthetic C_{ZZ} from the inversion results fit the observed C_{ZZ} well (Fig. 6h). $ZZ + RR$ waveform inversion recovers the source shapes better than *ZZ* waveform inversion.

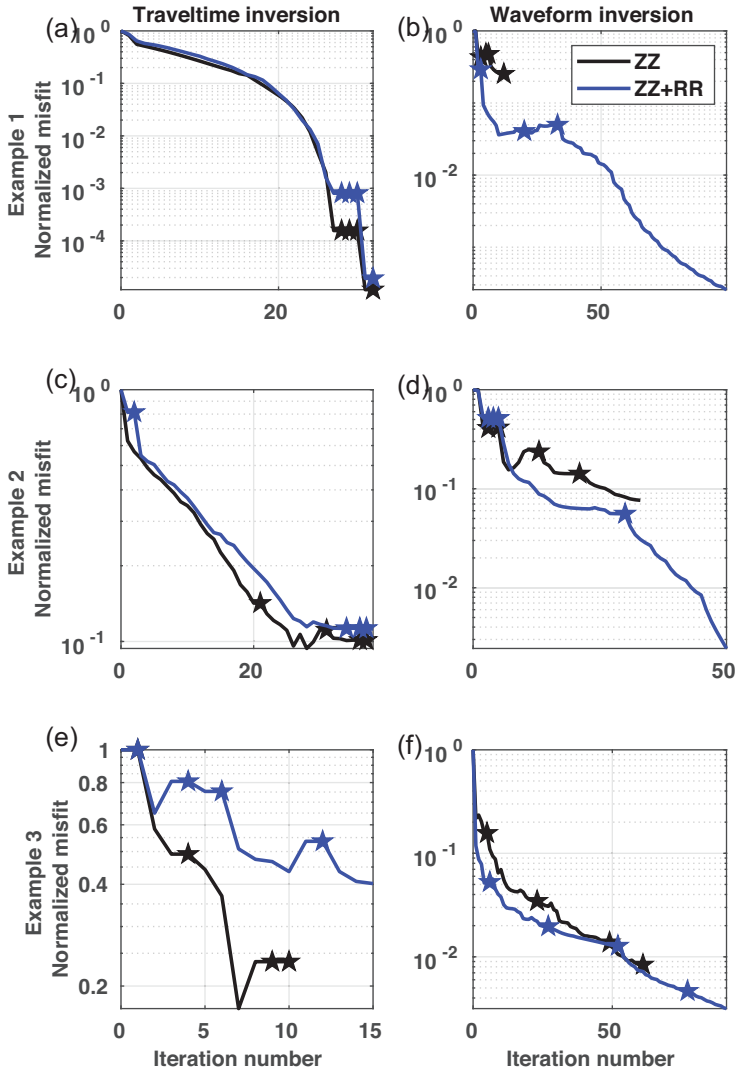

Figure 8. Traveltime and waveform inversion misfit comparisons. We show Example 1 (a and b), Example 2 (c and d), and Example 3 (e and f). The stars indicate when we extend the frequency bands (Table 2). We show the misfits over the whole frequency band, 2–16 Hz, relative to the initial misfit at each iteration.

4.3 Example 3: Sources outside of array

Seismic sources lie outside of the array in this example. Thus neither method perfectly recovers the source shape as in the two previous examples (Fig. 7). With the traveltime inversions, we determine that the inversion accurately provides an estimation of the directions of source locations, along with artefacts inside the array (Figs 7b and c), while the waveform inversion recovers the source location decently well (Figs 7e and f). Although the $ZZ + RR$ waveform inversion gives a similar result as the ZZ waveform inversion, the final misfit for $ZZ + RR$ is less than for ZZ (Fig. 8f).

4.4 Analysis of inversion results

We observe that in the traveltime inversion examples, multicomponent data do not help to resolve the source distribution. In Example 1, $ZZ + RR$ gives a simiar misfit over the whole frequency band (2–16 Hz) as ZZ (Fig. 8a). We ignore interpretation of Example 2 because the traveltime inversion does not work for this case as we explain in Section 4.2. When sources are outside of the array, $ZZ + RR$ gives a weaker artefact inside the array (Fig. 7c) than does ZZ, but still neither traveltime inversion gives a correct result.

The multicomponent data improve the waveform inversion in all three examples. $ZZ + RR$ better estimates the source shapes for in-array sources and gives lower misfits than ZZ regardless of whether sources are in the array or not (Figs 8b, d and f). In Example 3, we observe that $ZZ + RR$ provides a similar estimation of seismic source distribution and a close misfit to ZZ (Fig. 8f).

We also present seismic source estimation using matched-field processing (MFP) on the three examples (Fig. C1). The MFP results recover true source locations, but also many artefacts. We demonstrate that MFP is equivalent to a waveform source kernel where the initial

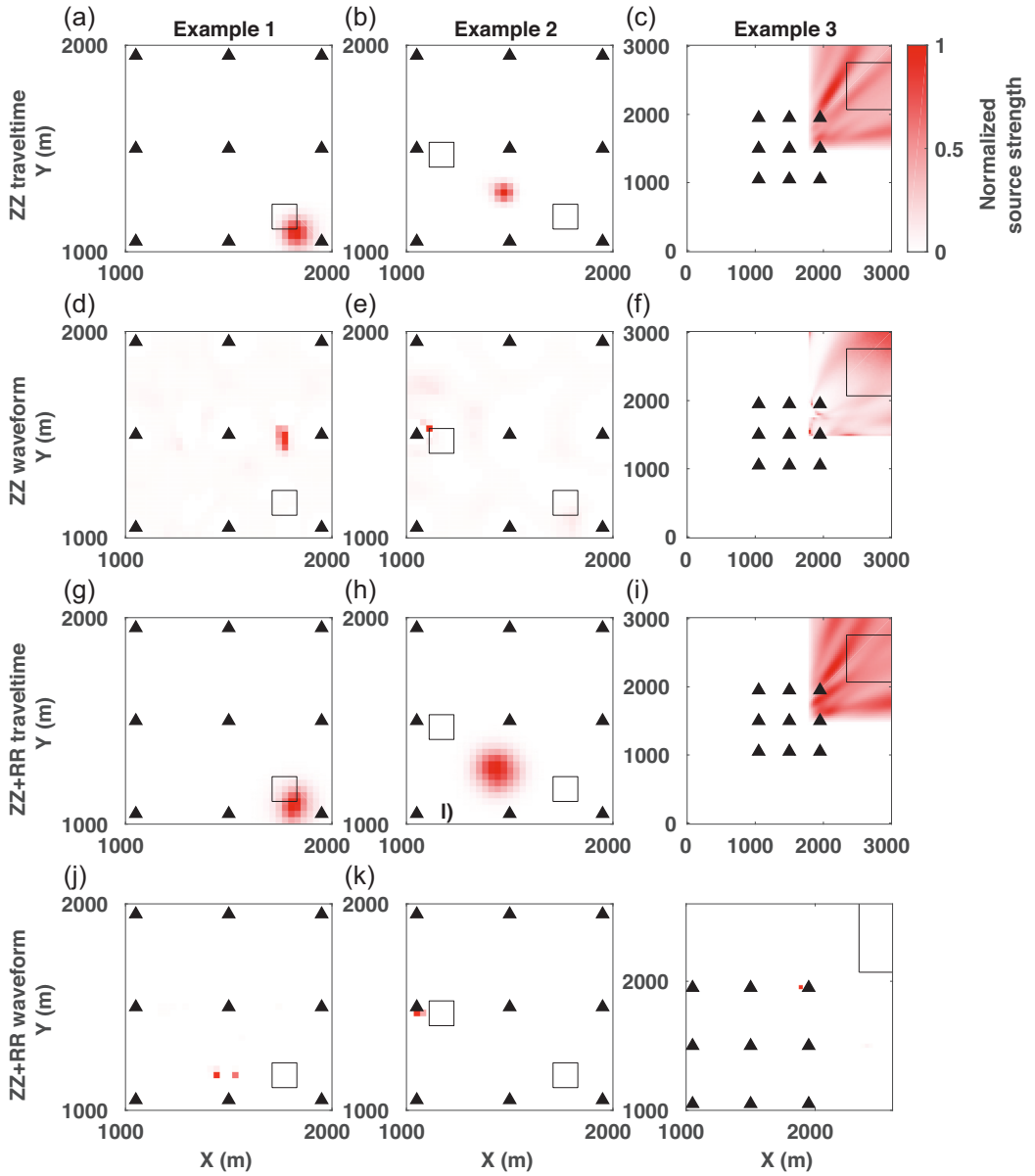

Figure 9. Source inversion results with a higher-velocity model (Table 1, Higher). The black empty squares indicate the shapes and locations of the true sources. We only show the Example 3 ZZ+RR waveform result in a certain area because the source locations from the inversion are within this area. The initial models are as same as in Section 4.

source strengths are zeros everywhere (Appendix C). These artefacts are suppressed by the waveform inversion and thus disappear in the inversion results (Figs 5e, 6e and 7e). One could use MFP results as an initial source model for the waveform inversion.

5 DISCUSSION

In this paper we introduce the theory needed to estimate source strength distribution from cross-correlations using multicomponent full-waveform inversion. We apply this theory to multicomponent field data in a companion paper, but here we comment on common data processing notions for completeness. To calculate ambient seismic noise cross-correlations, one usually adopts pre-processing procedures, such as time-domain normalization, frequency-domain normalization, or various stacking procedures (e.g. Shapiro *et al.* 2005; Yao *et al.* 2006). The normalization procedures change the cross-correlation waveforms and spectra (e.g. Bensen *et al.* 2007; Groos *et al.* 2012), as well as the apparent source strength distribution (e.g. Fichtner 2014). In order to estimate true source strengths, we do not use these normalization procedures. However, because the stacking procedure can mitigate random uncorrelated noise (e.g. Bensen *et al.* 2007), in real cross-correlations, stacking is used; keeping in mind that it is difficult to suppress the main source of noise in cross-correlations, which is localized correlated noise.

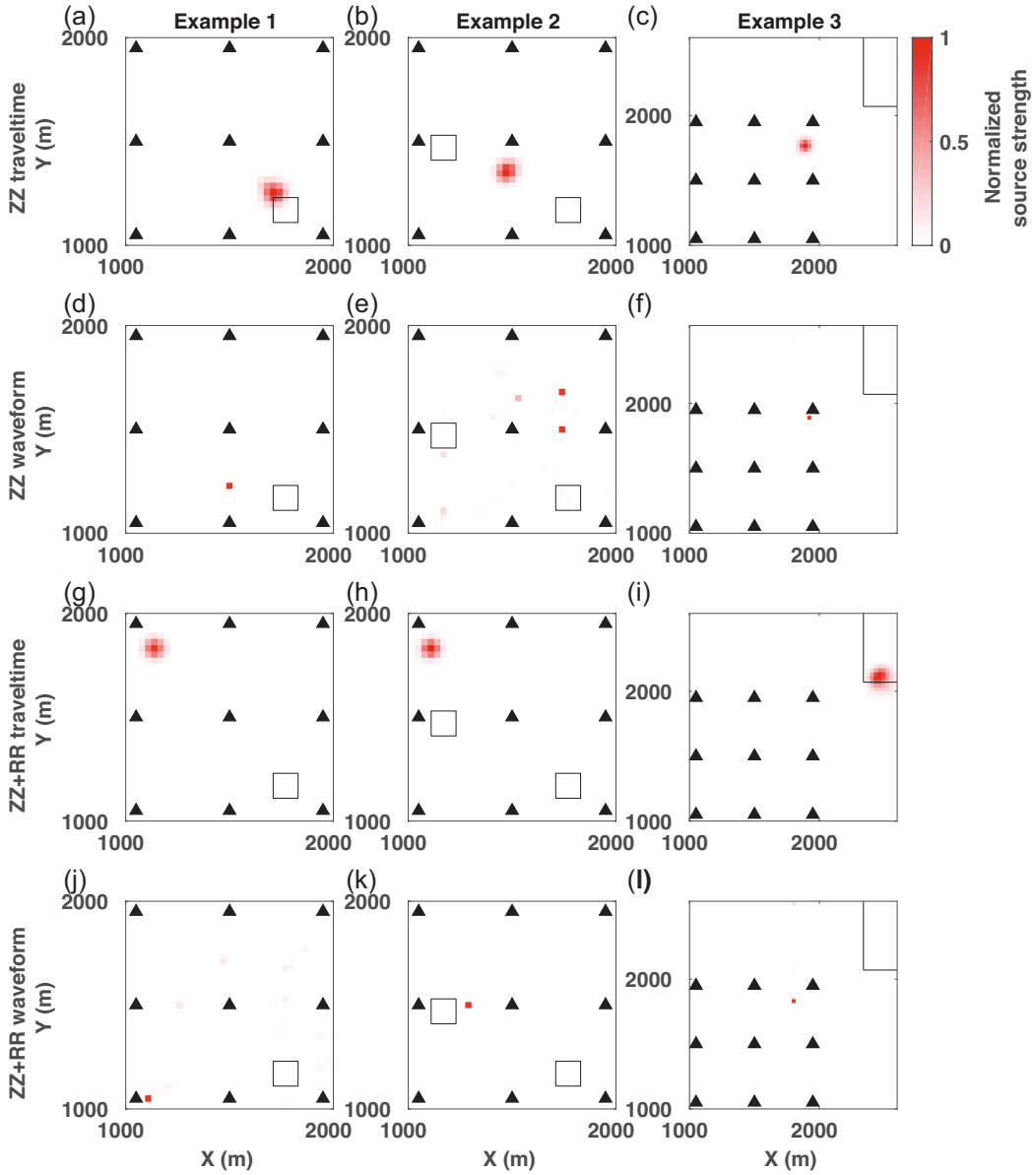

Figure 10. Source inversion results with a lower-velocity model (Table 1, Lower). The black empty squares indicate the shapes and locations of the true sources. We only show the Example 3 results in a certain area because the source locations from the inversion are within this area. The initial models are as same as in Section 4.

We present noise-free examples in this paper to demonstrate the physics of the problem and the properties of the adjoints. We address the topic of noise more thoroughly in our companion paper, noting that the quality of vertical- and horizontal-component data can be improved by burying receivers below the surface (e.g. Hutt *et al.* 2017). For clarity here, we present three simple examples of one or two seismic sources within or outside of the array. The maximum number of sources we can estimate depends on the chosen misfit function (i.e. traveltime or waveform), the array geometry (i.e. the number of sensors and the inter-sensor distance), and the complexity of the sources (if sources cancel each other, e.g. Wapenaar & Fokkema 2006; Halliday & Curtis 2008). Further study of the topic of how many sources can one locate is beyond the scope of this research.

We make four assumptions in the cross-correlation source distribution inversion procedure presented here:

(i) seismic sources are only distributed on the free surface;
(ii) seismic sources are independent from each other;
(iii) the subsurface velocity model is known;
(iv) the source spectral shapes are similar and known.

We make the first assumption because we are concerned with only fundamental mode Rayleigh waves (e.g. Halliday & Curtis 2008). Moreover, the ambient seismic noise >2 Hz is mainly due to human activity (e.g. Yamanaka *et al.* 1993) and composed of surface waves.

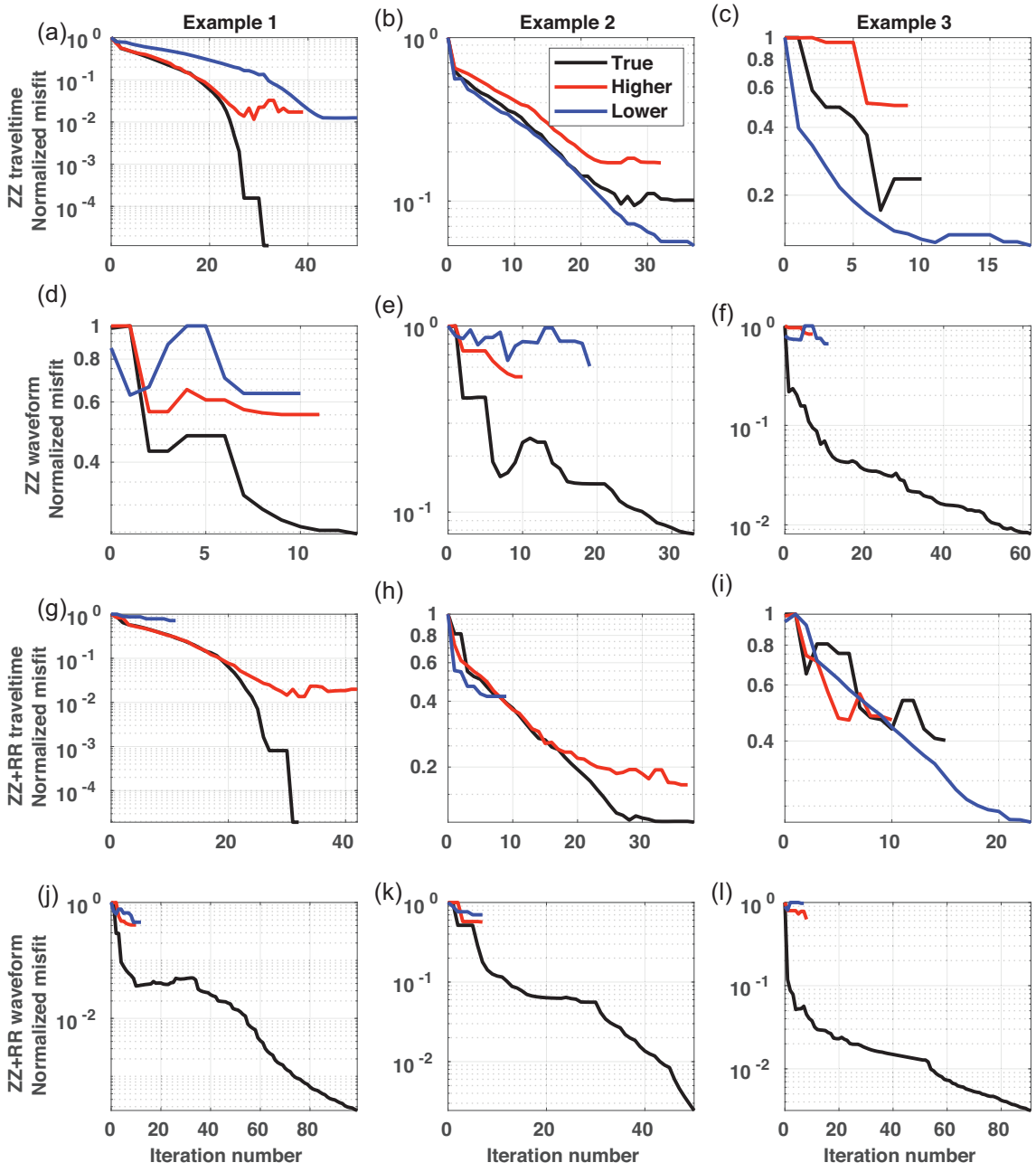

Figure 11. Traveltime and waveform inversion misfit curves with true, higher and lower velocity models (Table 1).

These seismic sources (e.g. traffic) usually occur on the surface or at shallow depths. We note that one could use the same theory and focus on body waves in the cross-correlations to locate seismic sources in depth. However, reverse-time migration is commonly used to locate the microseismic sources in depth (e.g. Artman *et al.* 2010), and we present the link between the cross-correlation source inversion and microseismic reverse-time migration in Appendix C. The second assumption is often made in seismic interferometry (e.g. Weaver & Lobkis 2001). We discuss the third assumption in this section, and a discussion of the fourth assumption is provided in our companion paper, which considers field data.

Biased subsurface velocity models have been shown to lead to biased source locations (e.g. Billings *et al.* 1994; Eisner *et al.* 2009). We use two incorrect velocity models (Table 1 Higher and Lower), where one has higher and the other has lower velocities than the true velocity model. We use the same data, the same inversion strategies and the same initial source models as in Section 4. We observe that we do not recover accurate source locations, shapes of source areas, nor the number of source areas with the incorrect velocity models (Figs 9 and 10). This phenomenon is expected because with these incorrect velocity models, the cross-correlations attribute the source to incorrect locations. For the same phase of a cross-correlation, $\omega(r_{As} - r_{Bs})/c$ in eq. (24), if we use an incorrect velocity, the $r_{As} - r_{Bs}$ will be larger or smaller than when using true velocity. Therefore the source inversion will place sources at the wrong locations (Figs 9 and 10).

We observe that the waveform inversion for all three synthetic data achieves the lowest final misfit with the true velocity model, as does the traveltime inversion for one source within the array (Fig. 11). This observation indicates that one can potentially estimate the source distribution and subsurface velocity structures through one inversion because the true source distribution and true subsurface velocities give a global minimum in the misfit function (Figs 11a, d, e and f). In practice, one estimates the source and velocity model iteratively (e.g. Lee *et al.* 2014) or simultaneously (e.g. Sager *et al.* 2018). We also observe that the multicomponent data, $ZZ + RR$, constrain the estimation better because the final normalized waveform misfit for the true velocity model is the smallest and for the incorrect velocity model is larger than ZZ.

6 CONCLUSION

We estimate the anisotropic source distribution of Rayleigh waves with vertical and multicomponent cross-correlation inversion in this paper. We assume that we know the subsurface structure. Through three synthetic examples, we show that multicomponent cross-correlations ($C_{ZZ} + C_{RR}$) do not help the traveltime inversion, but do help to resolve seismic source distributions more accurately than only the vertical cross-correlations (C_{ZZ}) in the waveform inversion. For the waveform inversion, both C_{ZZ} and $C_{ZZ} + C_{RR}$ provide accurate source distributions for seismic sources within array, while $C_{ZZ} + C_{RR}$ estimates the source shapes better. The $C_{ZZ} + C_{RR}$ waveform inversion gives a lower misfit than C_{ZZ} for sources within and outside of the array. We also note that the cross-correlation waveform inversion performs better than the traveltime inversion. If the initial source model is far from the true source distribution, the traveltime inversion can not fit the observed data, and thus gives biased estimations. The waveform inversion is more robust to the initial source model because the waveform inversion can fit complex observed waveforms with multiple arrivals. If sources are outside of array, the traveltime and waveform estimate rough directions instead of exact source shapes. Neither traveltime or waveform inversion works if the subsurface velocity model is incorrect. However, for the waveform inversion and the in-array one-source traveltime inversion, the true subsurface velocity model can give lower final misfit compared to incorrect velocity models. $C_{ZZ} + C_{RR}$ makes the waveform misfit difference even larger than C_{ZZ}, and thus better constrains estimation of the seismic source distribution and subsurface velocity model. The source inversion we use in this paper not only handles seismic sources located at the free surface, but also in depth.

ACKNOWLEDGEMENTS

ZX thanks D. Domenzain, J. Shragge, R. Snieder, G. A. Prieto and K. Sager for fruitful discussions. The authors thank editor Jean Virieux and reviewers Laura Ermert and Andreas Fichtner for their constructive comments that helped to improve this manuscript. This research is supported by the National Science Foundation under Grant No. 1643795 and by the Geological Society of America under Grant No. 11562-17. We acknowledge the high-performance computing support of the R2 compute cluster (DOI: 10.18122/B2S41H) provided by Boise State University Research Computing.

REFERENCES

Aki, K. & Richards, P.G., 2002. *Quantitative Seismology,* University Science Books.

Arai, H. & Tokimatsu, K., 2004. S-wave velocity profiling by inversion of microtremor H/V spectrum, *Bull. seism. Soc. Am.,* **94**(1), 53–63.

Ardhuin, F., Gualtieri, L. & Stutzmann, E., 2015. How ocean waves rock the Earth: two mechanisms explain microseisms with periods 3 to 300 s, *Geophys. Res. Lett.,* **42**(3), 765–772.

Artman, B., Podladtchikov, I. & Witten, B., 2010. Source location using time-reverse imaging, *Geophys. Prospect.,* **58**(5), 861–873.

Aster, R.C., Borchers, B. & Thurber, C.H., 2011. *Parameter Estimation and Inverse Problems,* Vol. **90,** Academic Press.

Bensen, G.D., Ritzwoller, M.H., Barmin, M.P., Levshin, A.L., Lin, F., Moschetti, M.P. & Yang, Y., 2007. Processing seismic ambient noise data to obtain reliable broad-band surface wave dispersion measurements, *Geophys. J. Int.,* **169**(3), 1239–1260.

Billings, S., Sambridge, M. & Kennett, B., 1994. Errors in hypocenter location: picking, model, and magnitude dependence, *Bull. seism. Soc. Am.,* **84**(6), 1978–1990.

Boaga, J., Cassiani, G., Strobbia, C.L. & Vignoli, G., 2013. Mode misidentification in Rayleigh waves: ellipticity as a cause and a cure, *Geophysics,* **78**(4), EN17–EN28.

Bozdağ, E., Trampert, J. & Tromp, J., 2011. Misfit functions for full waveform inversion based on instantaneous phase and envelope measurements, *Geophys. J. Int.,* **185**(2), 845–870.

Cheng, F. *et al.*, 2016. Multi-channel analysis of passive surface waves based on cross-correlations, *Geophysics,* **81**(5), EN57–EN66.

Chmiel, M., Roux, P., Herrmann, P., Rondeleux, B. & Wathelet, M., 2018. Data-based diffraction kernels for surface waves from convolution and correlation processes through active seismic interferometry, *Geophys. J. Int.,* **214**(2), 1468–1480.

Corciulo, M., Roux, P., Campillo, M., Dubucq, D. & Kuperman, W., 2012. Multiscale matched-field processing for noise-source localization in exploration geophysics, *Geophysics,* **77**(5), KS33–KS41.

Cros, E., Roux, P., Vandemeulebrouck, J. & Kedar, S., 2011. Locating hydrothermal acoustic sources at Old Faithful Geyser using matched field processing, *Geophys. J. Int.,* **187**(1), 385–393.

Dahlen, F., Hung, S.-H. & Nolet, G., 2000. Fréchet kernels for finite-frequency traveltimes–I. Theory, *Geophys. J. Int.,* **141**(1), 157–174.

Eisner, L., Duncan, P.M., Heigl, W.M. & Keller, W.R., 2009. Uncertainties in passive seismic monitoring, *Leading Edge,* **28**(6), 648–655.

Ermert, L., Sager, K., Afanasiev, M., Boehm, C. & Fichtner, A., 2017. Ambient seismic source inversion in a heterogeneous Earth—theory and application to the Earth's hum, *J. geophys. Res.: Solid Earth,* **122**(11), 9184–9207.

Fan, Y. & Snieder, R., 2009. Required source distribution for interferometry of waves and diffusive fields, *Geophys. J. Int.,* **179**(2), 1232–1244.

Fichtner, A., 2014. Source and processing effects on noise correlations, *Geophys. J. Int.,* **197**(3), 1527–1531.

Fichtner, A., 2015. Source-structure trade-offs in ambient noise correlations, *Geophys. J. Int.,* **202**(1), 678–694.

Fichtner, A., Kennett, B.L., Igel, H. & Bunge, H.-P., 2008. Theoretical background for continental-and global-scale full-waveform inversion in the time–frequency domain, *Geophys. J. Int.,* **175**(2), 665–685.

Fichtner, A., Stehly, L., Ermert, L. & Boehm, C., 2017. Generalised interferometry—I. Theory for inter-station correlations, *Geophys. J. Int.,* **208,** 603–638.

Gribler, G., Liberty, L.M., Mikesell, T.D. & Michaels, P., 2016. Isolating retrograde and prograde Rayleigh-wave modes using a polarity mute, *Geophysics,* **81**(5), V379–V385.

Groos, J., Bussat, S. & Ritter, J., 2012. Performance of different processing schemes in seismic noise cross-correlations, *Geophys. J. Int.,* **188**(2), 498–512.

Groos, L., Schäfer, M., Forbriger, T. & Bohlen, T., 2017. Application of a complete workflow for 2D elastic full-waveform inversion to recorded shallow-seismic Rayleigh waves, *Geophysics,* **82**(2), R109–R117.

Halliday, D. & Curtis, A., 2008. Seismic interferometry, surface waves and source distribution, *Geophys. J. Int.,* **175**(3), 1067–1087.

Haney, M.M. & Nakahara, H., 2014. Surface-wave Greens tensors in the near field, *Bull. seism. Soc. Am.,* **104**(3), 1578–1586.

Haney, M.M., Mikesell, T.D., van Wijk, K. & Nakahara, H., 2012. Extension of the spatial autocorrelation (SPAC) method to mixed-component correlations of surface waves, *Geophys. J. Int.,* **191**(1), 189–206.

Harmon, N., Rychert, C. & Gerstoft, P., 2010. Distribution of noise sources for seismic interferometry, *Geophys. J. Int.,* **183**(3), 1470–1484.

Hutt, C.R., Ringler, A.T. & Gee, L.S., 2017. Broadband seismic noise attenuation versus depth at the albuquerque seismological laboratorybroadband seismic noise attenuation versus depth at the albuquerque seismological laboratory, *Bull. seism. Soc. Am.,* **107**(3), 1402–1412.

Ishii, M., Shearer, P.M., Houston, H. & Vidale, J.E., 2005. Extent, duration and speed of the 2004 Sumatra–Andaman earthquake imaged by the Hi-Net array, *Nature,* **435**(7044), 933.

Johansen, H., 1977. A man/computer interpretation system for resistivity soundings over a horizontally strafified earth, *Geophys. Prospect.,* **25**(4), 667–691.

Juretzek, C. & Hadziioannou, C., 2016. Where do ocean microseisms come from? A study of Love-to-Rayleigh wave ratios, *J. geophys. Res.: Solid Earth,* **121**(9), 6741–6756.

Komatitsch, D. & Tromp, J., 2002. Spectral-element simulations of global seismic wave propagation-I. Validation, *Geophys. J. Int.,* **149**(2), 390–412.

Lee, E.-J., Chen, P., Jordan, T.H., Maechling, P.B., Denolle, M.A. & Beroza, G.C., 2014. Full-3-D tomography for crustal structure in southern California based on the scattering-integral and the adjoint-wavefield methods, *J. geophys. Res.: Solid Earth,* **119**(8), 6421–6451.

Liu, Q., Polet, J., Komatitsch, D. & Tromp, J., 2004. Spectral-element moment tensor inversions for earthquakes in southern California, *Bull. seism. Soc. Am.,* **94**(5), 1748–1761.

Luo, Y. & Schuster, G.T., 1991. Wave-equation traveltime inversion, *Geophysics,* **56**(5), 645–653.

Maggi, A., Tape, C., Chen, M., Chao, D. & Tromp, J., 2009. An automated time-window selection algorithm for seismic tomography, *Geophys. J. Int.,* **178**(1), 257–281.

Nakata, N., Chang, J.P., Lawrence, J.F. & Boué, P., 2015. Body wave extraction and tomography at Long Beach, California, with ambient-noise interferometry, *J. geophys. Res.: Solid Earth,* **120**(2), 1159–1173.

Nishida, K. & Fukao, Y., 2007. Source distribution of earth's background free oscillations, *J. geophys. Res.: Solid Earth,* **112**(B6), doi:10.1029/2006JB004720.

Rayleigh, L., 1885. On waves propagated along the plane surface of an elastic solid, *Proc. Lond. Math. Soc.,* **1**(1), 4–11.

Rhie, J. & Romanowicz, B., 2006. A study of the relation between ocean storms and the Earth's hum, *Geochem. Geophys. Geosyst.,* **7**(10), doi:10.1029/2006GC001274.

Rost, S. & Thomas, C., 2002. Array seismology: methods and applications, *Rev. Geophys.,* **40**(3), 2–1-2-27.

Sager, K., Ermert, L., Boehm, C. & Fichtner, A., 2018. Towards full waveform ambient noise inversion, *Geophys. J. Int.,* **212**(1), 566–590.

Shapiro, N.M., Michel, C., Laurent, S. & Ritzwoller, M.H., 2005. High-resolution surface-wave tomography from ambient seismic noise, *Science,* **307,** 1615–1618.

Snieder, R., 2004. Extracting the Green's function from the correlation of coda waves: a derivation based on stationary phase, *Phys. Rev. E,* **69**(4), 046610.

Tape, C., Liu, Q. & Tromp, J., 2007. Finite-frequency tomography using adjoint methods—methodology and examples using membrane surface waves, *Geophys. J. Int.,* **168**(3), 1105–1129.

Thorson, J.R. & Claerbout, J.F., 1985. Velocity-stack and slant-stack stochastic inversion, *Geophysics,* **50**(12), 2727–2741.

Tian, Y. & Ritzwoller, M.H., 2015. Directionality of ambient noise on the Juan de Fuca plate: implications for source locations of the primary and secondary microseisms, *Geophys. J. Int.,* **201**(1), 429–443.

Traer, J. & Gerstoft, P., 2014. A unified theory of microseisms and hum, *J. geophys. Res.: Solid Earth,* **119**(4), 3317–3339.

Tromp, J., Tape, C. & Liu, Q., 2005. Seismic tomography, adjoint methods, time reversal and banana-doughnut kernels, *Geophys. J. Int.,* **160**(1), 195–216.

Tromp, J., Luo, Y., Hanasoge, S. & Peter, D., 2010. Noise cross-correlation sensitivity kernels, *Geophys. J. Int.,* **18**(2), 791–819.

van Wijk, K., Mikesell, T.D., Schulte-Pelkum, V. & Stachnik, J., 2011. Estimating the Rayleigh-wave impulse response between seismic stations with the cross terms of the Green tensor, *Geophys. Res. Lett.,* **38**(16).

Virieux, J. & Operto, S., 2009. An overview of full-waveform inversion in exploration geophysics, *Geophysics,* **74**(6), WCC1–WCC26.

Wapenaar, K. & Fokkema, J., 2006. Greens function representations for seismic interferometry, *Geophysics,* **71**(4), SI33–SI46.

Weaver, R.L. & Lobkis, O.I., 2001. Ultrasonics without a source: thermal fluctuation correlations at MHz frequencies, *Phys. Rev. Lett.,* **87**(13), 134301.

Xu, Z. & Mikesell, T.D., 2017. On the reliability of direct rayleigh-wave estimation from multicomponent cross-correlations, *Geophys. J. Int.,* **210**(3), 1388–1393.

Xu, Z., Mikesell, T.D., Xia, J. & Cheng, F., 2017. A comprehensive comparison between the refraction microtremor and seismic interferometry methods for phase-velocity estimation, *Geophysics,* **82**(6), EN99–EN108.

Yamanaka, H., Dravinski, M. & Kagami, H., 1993. Continuous measurements of microtremors on sediments and basement in Los Angeles, California, *Bull. seism. Soc. Am.,* **83**(5), 1595–1609.

Yang, Y. & Ritzwoller, M.H., 2008. Characteristics of ambient seismic noise as a source for surface wave tomography, *Geochem. Geophys. Geosyst.,* **9**(2), 1256–1256.

Yao, H. & van Der Hilst, R.D., 2009. Analysis of ambient noise energy distribution and phase velocity bias in ambient noise tomography, with application to SE Tibet, *Geophys. J. Int.,* **179**(2), 1113–1132.

Yao, H., Van Der Hilst, R.D. & de Hoop, M.V., 2006. Surface wave array tomography in SE Tibet from ambient seismic noise and two-station analysis—I. Phase velocity maps, *Geophys. J. Int.,* **173**(1), 732–744.

APPENDIX A: TRAVELTIME ADJOINT SOURCES

We compute the perturbation of the traveltime misfit function (eq. 2) as:

$$\delta\chi = (T_{syn} - T_{obs})\delta(T_{syn} - T_{obs}) = (T_{syn} - T_{obs})\delta T, \tag{A1}$$

where $T = T_{syn} - T_{obs}$ represents the travel-time difference between synthetic and observed waveforms. Fichtner *et al.* (2017) derived an expression for δT. We present the main steps here. The travel-time difference, T, is measured by cross-correlation (Fig. A1) and is determined

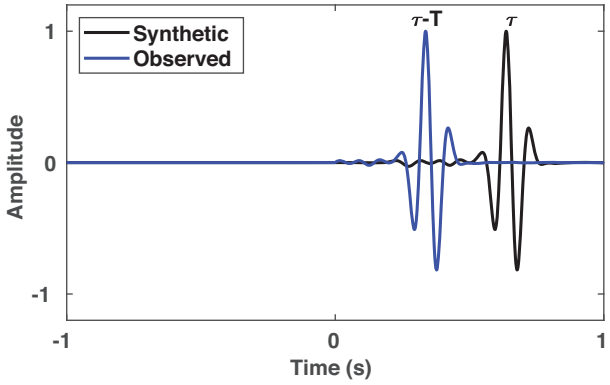

Figure A1. An illustration of the traveltime difference, T, between synthetic and observed cross-correlations.

as the cross-correlation maximum (e.g. Luo & Schuster 1991; Dahlen *et al.* 2000):

$$T = max\left[\int C_{mn}(r_A, r_B, \tau)[w(\tau - t)C^o_{mn}(r_A, r_B, \tau - t)]\mathrm{d}\tau\right], \tag{A2}$$

where $w(t)$ is a time window and C^o_{mn} is the observed data. The time derivative of the max function argument at $t = T$ is zero. Thus we can write

$$\int C_{mn}(r_A, r_B, \tau)\frac{\mathrm{d}}{\mathrm{d}t}[w(\tau - t)C^o_{mn}(r_A, r_B, \tau - t)]_{t=T}\mathrm{d}\tau = 0. \tag{A3}$$

We then write the traveltime perturbation to T and C_{mn} as:

$$\begin{aligned}&\int \delta C_{mn}(r_A, r_B, \tau)\frac{\mathrm{d}}{\mathrm{d}t}[w(\tau - t)C^o_{mn}(r_A, r_B, \tau - t)]_{t=T}\mathrm{d}\tau\\ &+ \int C_{mn}(r_A, r_B, \tau)\frac{\mathrm{d}^2}{\mathrm{d}t^2}[w(\tau - t)C^o_{mn}(r_A, r_B, \tau - t)]_{t=T}\delta T\,\mathrm{d}\tau = 0,\end{aligned} \tag{A4}$$

$$\rightarrow \delta T = -\frac{\int \delta C_{mn}(r_A, r_B, \tau)\frac{\mathrm{d}}{\mathrm{d}t}[w(\tau - t)C^o_{mn}(r_A, r_B, \tau - t)]_{t=T}\mathrm{d}\tau}{\int C_{mn}(r_A, r_B, \tau)\frac{\mathrm{d}^2}{\mathrm{d}t^2}[w(\tau - t)C^o_{mn}(r_A, r_B, \tau - t)]_{t=T}\mathrm{d}\tau}. \tag{A5}$$

One usually assumes that the observed waveform is a time-shifted copy of the synthetic waveform, $[w(\tau - t)C^o_{mn}(r_A, r_B, \tau - t)]_{t=T} = w(\tau)C_{mn}(r_A, r_B, \tau)$. In this case, we can rewrite the integrand of eq. (A5) as

$$\frac{\mathrm{d}}{\mathrm{d}t}[w(\tau - t)C^o_{mn}(r_A, r_B, \tau - t)]_{t=T} = -\frac{\mathrm{d}}{\mathrm{d}\tau}[w(\tau)C_{mn}(r_A, r_B, \tau)],$$

$$\text{and } \frac{\mathrm{d}^2}{\mathrm{d}t^2}[w(\tau - t)C^o_{mn}(r_A, r_B, \tau - t)]_{t=T} = \frac{\mathrm{d}^2}{\mathrm{d}\tau^2}[w(\tau)C_{mn}(r_A, r_B, \tau)].$$

Thus eq. (A5) becomes:

$$\delta T = \frac{\int \delta C_{mn}(r_A, r_B, \tau)\frac{\mathrm{d}}{\mathrm{d}\tau}[w(\tau)C_{mn}(r_A, r_B, \tau)]\mathrm{d}\tau}{\int C_{mn}(r_A, r_B, \tau)\frac{\mathrm{d}^2}{\mathrm{d}\tau^2}[w(\tau)C_{mn}(r_A, r_B, \tau)]\mathrm{d}\tau}, \tag{A6}$$

or in the frequency domain on a frequency band, $[\omega 1, \omega 2]$:

$$\delta T = i\frac{\int_{\omega 1}^{\omega 2}\omega\delta C_{mn}(r_A, r_B, \omega)[w(\omega) * C_{mn}(r_A, r_B, \omega)]^*\mathrm{d}\omega}{\int_{\omega 1}^{\omega 2}\omega^2 C_{mn}(r_A, r_B, \omega)[w(\omega) * C_{mn}(r_A, r_B, \omega)]^*\mathrm{d}\omega}. \tag{A7}$$

Finally, we write eq. (A7) with an adjoint source (f) for a single frequency (ω)

$$\delta T = \int_{\omega 1}^{\omega 2} f(\omega)\delta C_{mn}(r_A, r_B, \omega)\mathrm{d}\omega, \tag{A8}$$

where

$$f(\omega) = i\frac{\omega[w(\omega) * C_{mn}(r_A, r_B, \omega)]^*}{\int_{\omega 1}^{\omega 2}\omega^2 C_{mn}(r_A, r_B, \omega)[w(\omega) * C_{mn}(r_A, r_B, \omega)]^*\mathrm{d}\omega}. \tag{A9}$$

If we assume that we know the Green's functions (eq. 4), we can write

$$\delta T = \int_{\omega 1}^{\omega 2}\int_V G_{mp}(r_A, r_s, \omega)G^*_{np}(r_B, r_s, \omega)f(\omega)\delta S_p(r_s, \omega)\mathrm{d}r_s\mathrm{d}\omega, \tag{A10}$$

and we can write the source kernel for δT as

$$K_{mn}(\omega, r_s) = G_{mp}(r_A, r_s, \omega)G^*_{np}(r_B, r_s, \omega)f(\omega). \tag{A11}$$

eq. (A11) does not require observed data. Thus we use eq. (A11) in Section 3 to analyse the traveltime source kernels. This formulation assumes that the observed waveform is close to the synthetic waveform. As the assumption is not valid in our synthetic data examples, we do not adopt eq. (A11) in the actual inversion algorithm.

In the traveltime inversions (Sections 4 and 5), we combine the kernel eq. (A11) with eq. (A1) as:

$$\begin{aligned} K^o_{mn}(\omega, r_s) &= (T_{syn} - T_{obs})K_{mn}(\omega, r_s) \\ &= (T_{syn} - T_{obs})G_{mp}(r_A, r_s, \omega)G^*_{np}(r_B, r_s, \omega)f(\omega). \end{aligned} \tag{A12}$$

APPENDIX B: WAVEFORM ADJOINT SOURCES

We write the perturbation of the waveform misfit function (eq. 1) following Fichtner *et al.* (2017):

$$\delta\chi = \int [w^2(t)(C_{mn}(r_A, r_B, t) - C^o_{mn}(r_A, r_B, t))]\delta C_{mn}(r_A, r_B, t)\mathrm{d}t \tag{B1}$$

$$= \frac{1}{2\pi}\int [w(\omega) * w(\omega) * (C_{mn}(r_A, r_B, \omega) - C^o_{mn}(r_A, r_B, \omega))]^*\delta C_{mn}(r_A, r_B, \omega)\mathrm{d}\omega, \tag{B2}$$

where $\delta C^o_{mn}(r_A, r_B, \omega) = 0$. The corresponding adjoint source is defined as

$$f(\omega) = \frac{1}{2\pi}[w(\omega) * w(\omega) * (C_{mn}(r_A, r_B, \omega) - C^o_{mn}(r_A, r_B, \omega))]^*. \tag{B3}$$

In Section 3 where there is no observed cross-correlation, we write the adjoint source as (Fichtner *et al.* 2017)

$$f(\omega) = \frac{1}{2\pi}[w(\omega) * w(\omega) * C_{mn}(r_A, r_B, \omega)]^*. \tag{B4}$$

APPENDIX C: THE LINK AMONG WAVEFORM SOURCE INVERSION, MATCHED-FIELD PROCESSING AND REVERSE-TIME MIGRATION

We can relate the waveform source inversion with the matched-field processing. If we assume that there are no seismic sources in the initial source distribution model, $C_{mn}(r_A, r_B, \omega)$ will be equal to zero. We can write the waveform source equation by combining eqs (9) and (B2) as

$$\delta\chi = -\frac{1}{2\pi}\int\int_V [C^o_{mn}(r_A, r_B, \omega)]^* G_{mp}(r_A, r_s, \omega)G^*_{np}(r_B, r_s, \omega)\delta S_p(r_s, \omega)\mathrm{d}r_s\mathrm{d}\omega, \tag{C1}$$

where we neglect the time window term $w(\omega)$. We then rewrite the observed cross-correlation, $C^o_{mn}(r_A, r_B, \omega) = U^o_m(r_A, \omega)[U^o_n(r_B, \omega)]^*$, where $U^o_m(r_A, \omega)$ is the observed m-direction component seismic recording at r_A. The cross-correlation at a single frequency is a component of the cross-spectral density matrix in matched-field processing (e.g. Cros *et al.* 2011). We now write the source kernel in eq. (C1) explicitly as

$$K = -[U^o_m(r_A, \omega)]^* U^o_n(r_B, \omega)G_{mp}(r_A, r_s, \omega)G^*_{np}(r_B, r_s, \omega), \tag{C2}$$

and rewrite eq. (C1) as

$$\delta\chi = -\frac{1}{2\pi}\int\int_V K\delta S_p(r_s, \omega)\mathrm{d}r_s\mathrm{d}\omega. \tag{C3}$$

In practice, we stack the kernel among all sensor pairs and the stacked kernel reads as

$$K = -\sum_{r_A r_B}[U^o_m(r_A, \omega)]^* U^o_n(r_B, \omega)G_{mp}(r_A, r_s, \omega)G^*_{np}(r_B, r_s, \omega). \tag{C4}$$

We can recognize the stacked kernel is a conjugation of the linear (Bartlett) processor in matched-field processing (e.g. Cros *et al.* 2011; Corciulo *et al.* 2012) without autocorrelation terms:

$$\sum_{r_A r_B} G^*_{zz}(r_A, r_s, \omega)U^o_z(r_A, \omega)[U^o_z(r_B, \omega)]^* G_{zz}(r_B, r_s, \omega), \tag{C5}$$

where people usually use vertical component (Z) data. Therefore the matched-field processing results are similar to the stacked waveform source kernels where the initial source strengths are zero. We apply the matched-field processing to the ZZ data in Section 4 and estimate the seismic source strengths shown in Fig. C1. We calculate the Rayleigh-wave phase velocity for the halfspace model (Table 1 True), 1391 m s^{-1} (Rayleigh 1885). We use eq. (23) as the Green's function in MFP (eq. C5) and estimate source distributions for each example in Section 4 (Figs C1a, b and c). We observe that high source strength values concentrate near the sensors and the true source locations. The singularities

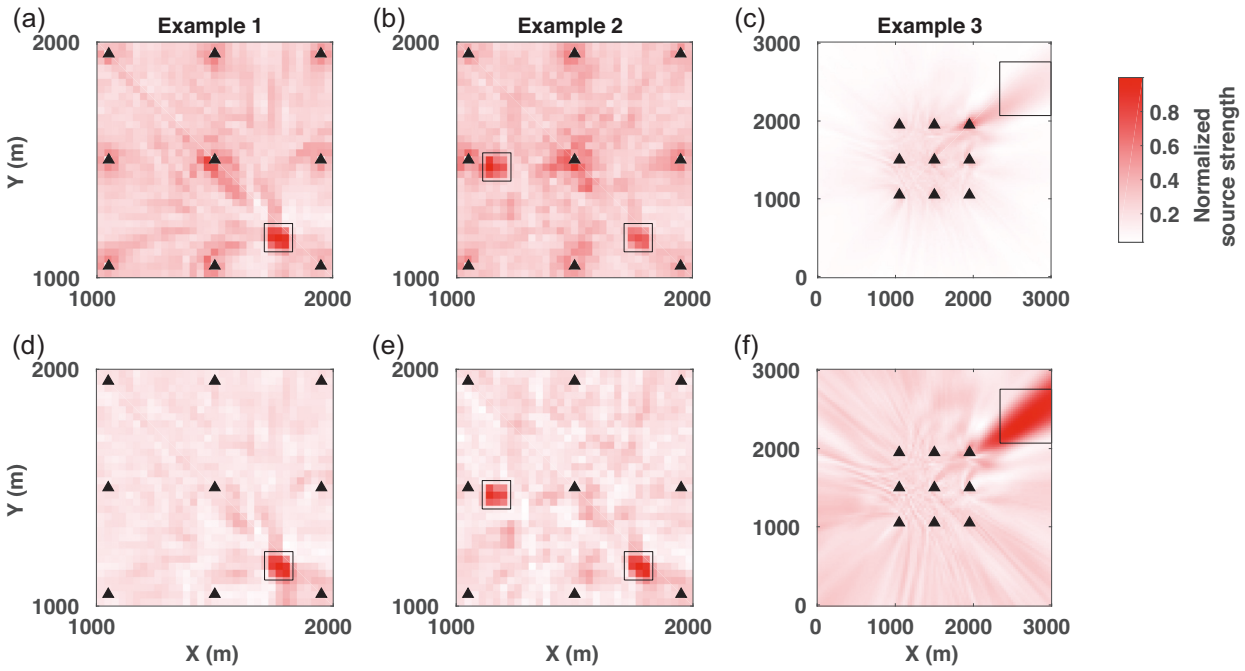

Figure C1. Matched-field processing (MFP) results from the *ZZ* data in Section 4. We use the full Rayleigh-wave Green's function (eq. 23) in MFP (a, b and c), and we only use the phase part of the Green's function (eq. 23) in MFP (d, e and f). The black empty squares indicate the shapes and locations of the true sources.

at the sensors are due to the amplitude term in the Green's function, $\sqrt{\frac{1}{8\pi\omega r/c}}$. If we also only use the phase part of the Green's function, the singularities disappear (Figs C1d, e and f). The singularity also exists in the waveform inversion and that is why people adopt a taper near sources and receivers or smooth the gradient (e.g. Groos *et al.* 2017).

We can also relate this kernel (eq. C2) to reverse-time migration. If we assume that $C^o_{mn}(r_A, r_B, \omega)$ is due to a microseismic or secondary source, r', we can write the kernel as

$$K = [C^o_{mn}(r_A, r_B, \omega)]^* G_{mp}(r_A, r_s, \omega) G^*_{np}(r_B, r_s, \omega) \tag{C6}$$

$$= [U^o_m(r_A, r', \omega)]^* U^o_n(r_B, r', \omega) G_{mp}(r_A, r_s, \omega) G^*_{np}(r_B, r_s, \omega) \tag{C7}$$

$$= [U_m(r_A, r', \omega) G^*_{mp}(r_A, r_s, \omega)]^* [U_n(r_B, r', \omega) G^*_{np}(r_B, r_s, \omega)]. \tag{C8}$$

We recognize that the kernel, eq. (C8), is the microseismic imaging condition [e.g. Artman *et al.* 2010, eq. (4)] in the frequency domain. Therefore the imaging condition in reverse-time migration is similar to the waveform source kernel with zero initial source strength.

APPENDIX D: FOURIER TRANSFORM CONVENTION

We use the following Fourier transform convention

$$U(\omega) = \int_{-\infty}^{\infty} u(t) e^{-i\omega t} \mathrm{d}t, \tag{D1}$$

as opposed to

$$U(\omega) = \int_{-\infty}^{\infty} u(t) e^{i\omega t} \mathrm{d}t \tag{D2}$$

(e.g. Aki & Richards 2002; Haney & Nakahara 2014).